

Heterochromatin drives compartmentalization of inverted and conventional nuclei

Martin Falk^{1,8}, Yana Feodorova^{2,3,8}, Natalia Naumova^{4,5,8}, Maxim Imakaev¹, Bryan R. Lajoie^{4,6}, Heinrich Leonhardt³, Boris Joffe³, Job Dekker⁴, Geoffrey Fudenberg^{1,7*}, Irina Solovei^{3*} & Leonid A. Mirny^{1*}

The nucleus of mammalian cells displays a distinct spatial segregation of active euchromatic and inactive heterochromatic regions of the genome^{1,2}. In conventional nuclei, microscopy shows that euchromatin is localized in the nuclear interior and heterochromatin at the nuclear periphery^{1,2}. Genome-wide chromosome conformation capture (Hi-C) analyses show this segregation as a plaid pattern of contact enrichment within euchromatin and heterochromatin compartments³, and depletion between them. Many mechanisms for the formation of compartments have been proposed, such as attraction of heterochromatin to the nuclear lamina^{2,4}, preferential attraction of similar chromatin to each other^{1,4–12}, higher levels of chromatin mobility in active chromatin^{13–15} and transcription-related clustering of euchromatin^{16,17}. However, these hypotheses have remained inconclusive, owing to the difficulty of disentangling intra-chromatin and chromatin–lamina interactions in conventional nuclei¹⁸. The marked reorganization of interphase chromosomes in the inverted nuclei of rods in nocturnal mammals^{19,20} provides an opportunity to elucidate the mechanisms that underlie spatial compartmentalization. Here we combine Hi-C analysis of inverted rod nuclei with microscopy and polymer simulations. We find that attractions between heterochromatic regions are crucial for establishing both compartmentalization and the concentric shells of pericentromeric heterochromatin, facultative heterochromatin and euchromatin in the inverted nucleus. When interactions between heterochromatin and the lamina are added, the same model recreates the conventional nuclear organization. In addition, our models allow us to rule out mechanisms of compartmentalization that involve strong euchromatin interactions. Together, our experiments and modelling suggest that attractions between heterochromatic regions are essential for the phase separation of the active and inactive genome in inverted and conventional nuclei, whereas interactions of the chromatin with the lamina are necessary to build the conventional architecture from these segregated phases.

To test mechanisms of genome compartmentalization, we performed Hi-C in four mouse cell types that were isolated from primary tissues. These cell types have either conventional or inverted nuclear architectures: rod photoreceptors (inverted), non-rod retinal neurons (conventional), wild-type thymocytes (conventional) and lamin B receptor-null (*Lbr*^{-/-}) thymocytes^{20,21} (inverted) (Fig. 1a); data were collected from two biological replicates for each tissue type (Extended Data Fig. 1 and Supplementary Table 1). The latter three cell types provide points of comparison to rods: retinal non-rod neurons are similarly post-mitotic cells but have large conventional nuclei; wild-type and *Lbr*^{-/-} thymocytes are actively cycling cells with nuclei of a size similar to the nuclei of rods. Nuclear inversion of *Lbr*^{-/-} thymocytes is incomplete, most likely owing to regular cell divisions (Extended Data Fig. 2). Despite the large differences in nuclear organization that are evident from

microscopy (Fig. 1a), all features of chromatin organization characteristic of conventional nuclei—topologically associating domains (TADs), chromosome territories and compartments—are present in inverted nuclei, although with quantitative differences (Fig. 1b and Extended Data Figs. 3, 4, 5), as has also been seen recently in single-cell Hi-C²².

We subsequently investigated whether major differences in spatial positioning of euchromatin and heterochromatin affect nuclear compartmentalization as seen in Hi-C. We computed compartment profiles from Hi-C maps²³ (Fig. 1b) and defined the degree of compartmentalization as the enrichment of contacts between compartments of the same type (Methods). Although assignments of individual regions to euchromatic (A) and heterochromatic (B) compartments generally depend on the cell type, compartment profiles are highly correlated before and after perturbing the association of chromatin with the lamina in thymocytes—approaching the correlation between biological replicates (Extended Data Fig. 5b–e). The degree of compartmentalization decreases only slightly in thymocytes upon inversion, but becomes stronger in rods (Fig. 1c and Extended Data Fig. 5f). Together, our analyses show that the degree of compartmentalization is preserved despite the altered spatial positioning of individual A or B compartments upon inversion (Fig. 1a, d), and suggest that mechanisms of compartmentalization cannot be strictly dependent on the nuclear lamina.

To reconcile the similar Hi-C compartmentalization of inverted and conventional nuclei with the different spatial geometries in these nuclei, we sought a mechanism of compartmentalization that satisfied the three following criteria. First, it should reproduce the inverted organization, defined quantitatively with microscopy by the radial positions of different types of chromatin and with Hi-C by the strength of compartmentalization. Second, it should reproduce the conventional organization when attractive interactions between heterochromatin and the nuclear lamina are introduced. The conventional organization is characterized by a similar degree of compartmentalization in Hi-C, but a markedly different spatial location of compartments in microscopy. Third, it should be based on forces that are biologically and physically plausible. This limited us to short-range attractions between different chromatin types and of chromatin to the nuclear lamina.

To test mechanisms of compartmentalization, we developed an equilibrium polymer model of chromatin that represents chromosomes as block copolymers (Fig. 2a), similar to other phase-separation models of compartmentalization^{4–7}. Extending previous two-type models, our simulations use three types of monomers: euchromatin (A), heterochromatin (B) and pericentromeric constitutive heterochromatin (C). We modelled eight chromosomes—each consisting of 6,000 monomers; each monomer representing 40 kb of chromatin—confined to a spherical nucleus at 35% volume density²⁴. The sequence of A and B monomers along the polymer mirrors the sequence of compartments derived from Hi-C data of rods (Fig. 2a and Methods). To represent the satellite repeats of a pericentromeric region²⁵—or chromocentre—which

¹Institute for Medical Engineering and Science, and Department of Physics, Massachusetts Institute of Technology, Cambridge, MA, USA. ²Department of Medical Biology, Medical University–Plovdiv, Plovdiv, Bulgaria. ³Biozentrum, Ludwig Maximilians University Munich, Planegg-Martinsried, Germany. ⁴Howard Hughes Medical Institute, and Program in Systems Biology, Department of Biochemistry and Molecular Pharmacology, University of Massachusetts Medical School, Worcester, MA, USA. ⁵Epinomics Inc, Menlo Park, CA, USA. ⁶Illumina Inc, San Diego, CA, USA. ⁷Gladstone Institutes of Data Science and Biotechnology, University of California, San Francisco, San Francisco, CA, USA. ⁸These authors contributed equally: Martin Falk, Yana Feodorova, Natalia Naumova.
*e-mail: geoff.fudenberg@gmail.com; irina.solovei@lrz.uni-muenchen.de; leonid@mit.edu

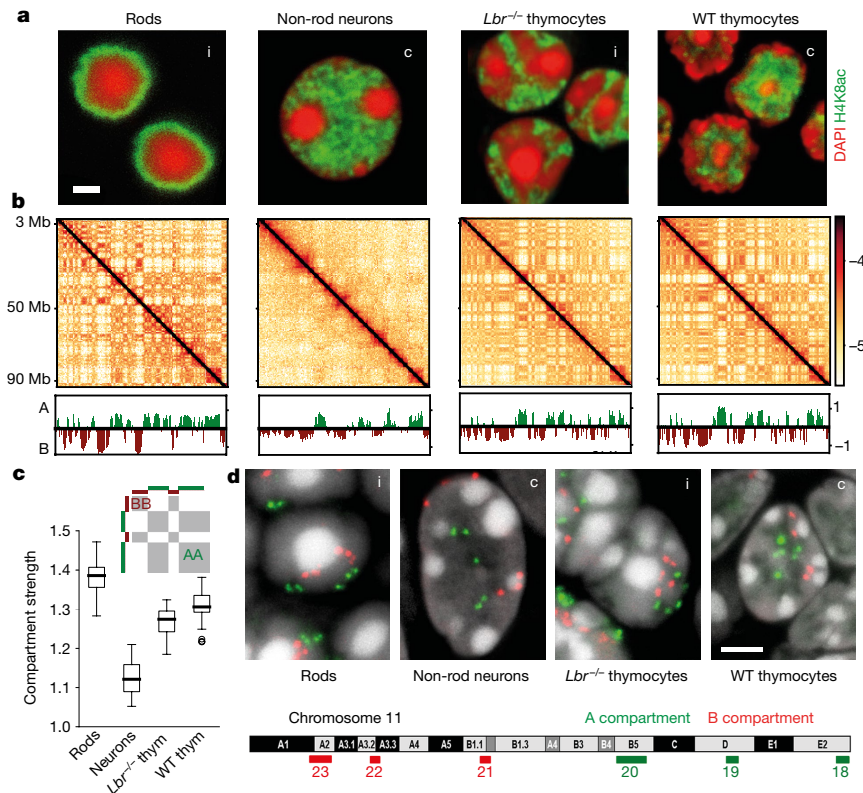


Fig. 1 | Microscopy and Hi-C analysis of conventional and inverted nuclei. **a**, Nuclei of non-rod neurons and wild-type (WT) thymocytes are conventional (c) with euchromatin residing in the interior. Rod nuclei are inverted (i) with a single central heterochromatic region (including the chromocentre) and euchromatin forming the peripheral shell. Nuclei of *Lbr*^{-/-} thymocytes are partially inverted and have several chromocentres. Euchromatin staining with anti-H4K8ac antibody (green); counterstain with DAPI (red), highlighting heterochromatin. Images are single optical sections. Scale bar, 2 μ m. See Extended Data Figs. 9a, 10a for schematic of positioning of euchromatin, heterochromatin and chromocentres. **b**, Hi-C contact maps (\log_{10} (contact frequency)) for an 87-Mb region of chromosome 1 (mm9) and corresponding compartment profiles indicating regions in the A (green) and B (red) compartment (see also Extended Data Fig. 1). Maps are corrected using ICE²³, with the matrix sums normalized to 1 (Methods). **c**, Compartmentalization is

strongest in rods and weakest in non-rod neurons; schematic indicates how compartmentalization is quantified ((AA + BB)/total). Box plots show compartmentalization calculated separately for each autosome in two replicates. Centre line is the median, the box ranges from the lower to upper quartiles and whiskers extend to 1.5 \times the interquartile range (see also Extended Data Fig. 5). **d**, Flipped localization of A and B compartment loci on chromosome 11 in inverted compared to conventional nuclei. Positions of detected compartments are marked with green (A compartment) and red (B compartment) bars below the chromosome ideogram. Fluorescence in situ hybridization (FISH) with a bacterial artificial chromosome (BAC) cocktail probe; BAC numbers are indicated below the compartment loci. Note the chromocentres are shown as bright globules in DAPI staining. Images are projections of 3- μ m confocal stacks. Scale bar, 2 μ m. The experiment was repeated twice.

is unmappable by Hi-C, we place a block of C monomers (16% of the chromosome length) at the proximal end of each chromosome. All monomers have excluded volume, and experience short-range pairwise attraction depending on their chromatin type. Given six pairwise attraction parameters (A–A, A–B, B–B, B–C, C–C and A–C), all possible permutations of attraction strengths specify 720 (6!) classes of models (see Methods). To constrain the space of possible models, we first quantitatively compared all 720 classes of models to microscopy data. Specifically, we computed the radial distributions for A, B and C monomers, and compared the distributions obtained in simulations with those obtained in microscopy¹⁹ (Fig. 2b and Methods).

Most model classes do not agree with the concentric geometry of the inverted nucleus observed in microscopy (Fig. 2c). For example, overly strong B–C interactions cause B and C to mix (Fig. 2c, model 8 and Extended Data Fig. 6a–c), while relatively weak B–C interactions lead to the expulsion of the C monomer chromocentres from a central mass of B monomers (Fig. 2c, model 112). Overly strong A–A interactions tend to encourage the formation of large euchromatic globules (Fig. 2c, model 650 and Extended Data Fig. 6d–f). Notably, this result argues against activity-related clustering of euchromatic regions^{13–16} as the main mechanism that underlies compartmentalization.

Only eight classes of models could reproduce the experimentally observed inverted geometry (Fig. 2b, c). These eight classes follow a

particular ordering of interaction strengths, which are, on average, dominated by heterochromatin interactions: A–A \approx A–B $<$ A–C $<$ B–B $<$ B–C $<$ C–C (Fig. 2d). We focused on the best-fitting class of models and further simplified these models by fixing C–C to be high enough to induce a central globule of C monomers, A–A to always be much smaller than B–B (Extended Data Fig. 7d), and all cross-terms to be the geometric means of the respective pure terms (for example, A–B = (A–A \times B–B)^{1/2}), thus satisfying the Flory–Huggins phase separation criterion²⁶. This leaves the B–B attraction as the only free parameter.

We next tested whether the heterochromatin-dominated models that reproduced the inverted organization seen in microscopy images could simultaneously reproduce the compartmentalization observed in Hi-C data. Fixing the order of interaction strengths, we found a range of the B–B attraction energies for which models could quantitatively reproduce both Hi-C and microscopy data (Fig. 3a, b). The central role of attractions between heterochromatic regions revealed by our analyses of inverted nuclei contrasts with suggestions that hinge on the importance of interactions between euchromatic regions^{13–16} or with the lamina² as the main drivers of compartmentalization. Stronger attractions between heterochromatic regions is consistent with the recently observed dominant role of heterochromatin-associated histone methylation in determining the mechanical properties of chromosomes²⁷.

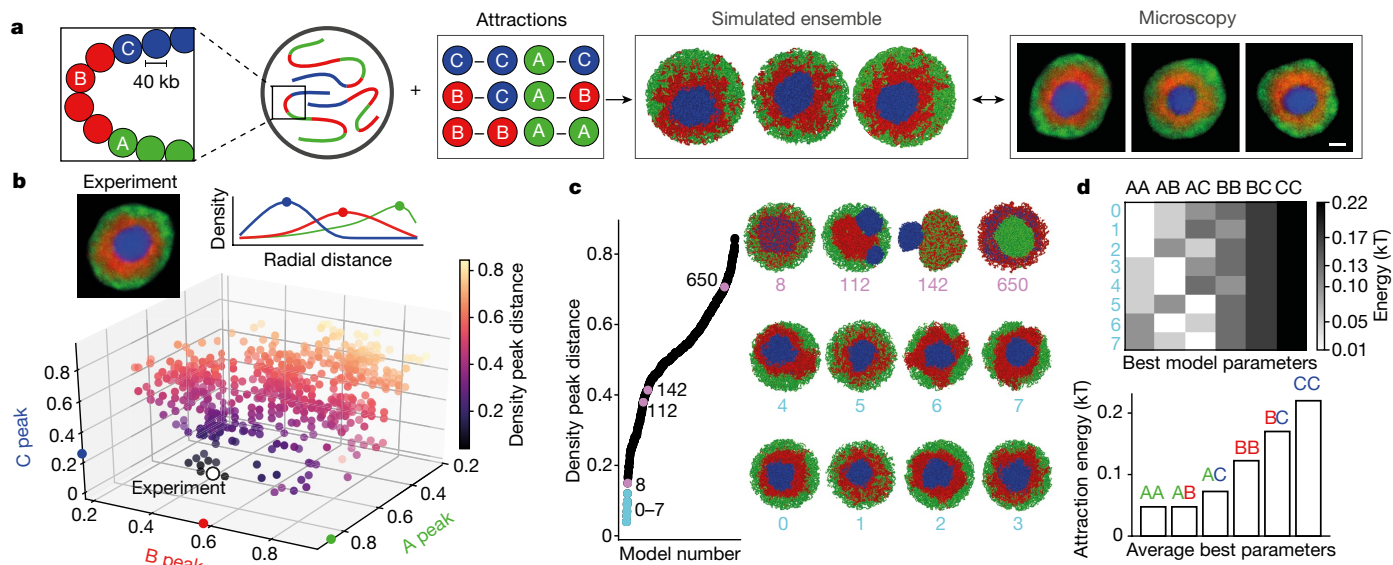


Fig. 2 | Morphology of the inverted nucleus restricts possible models of compartmentalization. **a**, Our approach was to first define mechanistic polymer models with parameters that describe the chromatin interactions between three types of monomers (A for euchromatin, B for heterochromatin and C for constitutive heterochromatin). Second, we simulated an ensemble of conformations for each model via Langevin dynamics. Finally, we compared simulations with experiments. To compare to microscopy, we computed radial distributions of A, B and C monomers. Models are characterized by relative attraction strengths between every pair of monomer types, leading to 720 (6!) classes of models. For analysis and other models, see Extended Data Fig. 6. Scale bar, 1 μm . **b**, Quantitative comparison of 720 model classes with microscopy

To extend our model to conventional nuclei, we represented heterochromatin–lamina interactions with a short-ranged attraction^{2,20} (B–Lam attraction, Fig. 3c, d). To model the distinct chromocentres that were found experimentally, we pinned C-monomer clusters to random positions along the lamina. Pinning is not necessary to maintain distinct chromocentres for a period of time, but is needed to keep them separated in equilibrium simulations (Supplementary Video 1). By sweeping B–B and B–Lam attractions, we found that our model could simultaneously reproduce both the spatial positioning of active and inactive chromatin as observed in microscopy images, and the compartmentalization observed in Hi-C data for wild-type thymocytes. Whereas reproducing microscopy data requires sufficiently strong B–Lam without further constraining these parameters, simultaneously reproducing the compartmentalization observed in Hi-C data narrows down the range of B–Lam and B–B attractions (Fig. 3c, d). Notably, the region of best-fitting B–B attraction for conventional nuclei includes the best-fitting B–B attraction for inverted nuclei. As histone modifications remain associated with the same type of chromatin in inverted and conventional nuclei^{20,21}, we parsimoniously assume that B–B attraction remains the same in both nuclear types. With this constraint, we can narrow the range of possible B–Lam values (approximately 0.3 kT; Fig. 3c) and find that B–Lam attraction should be comparable to B–B attraction. Together, our simulations indicate that compartmentalization in both inverted and conventional nuclei is primarily controlled by heterochromatin–heterochromatin attractions, whereas heterochromatin–lamina attraction controls the global spatial morphology.

To test our proposed mechanism of compartmentalization, we simulated a time course of nuclear inversion (Fig. 4a, b). For this, we turned off lamina–heterochromatin interactions in simulated conventional nuclei and observed spontaneous inversion (Fig. 4b). Notably, the simulated time course mirrored key events during rod differentiation *in vivo*^{19,20} (Fig. 4b). B and C monomer droplets underwent irreversible liquid-like fusion in simulations, similar to other phase-separated systems^{10,11} (Fig. 4b, Extended Data Fig. 8a, c and Supplementary Video 2).

using the density peak distance, measuring the Euclidean distance between the peaks of the radial distributions for each chromatin class in simulations and experiment (white dot). Simulated densities computed from 50 configurations, experimental data from 24 nuclei¹⁹. **c**, Arranging the 720 models according to agreement with experimental data (that is, density peak distance; see Methods). The best eight models (0–7) are indicated in cyan. Other models are plotted in black, or pink, if a representative conformation is shown from that model. Models 8–15 are shown in Extended Data Fig. 6a. **d**, Heat map (top, individual models) and bar plot (bottom, averaged) of the best eight model parameters show that they increase on average as A–A \approx A–B < A–C < B–B < B–C < C–C.

In simulations, although compartmentalization transiently dips after heterochromatin moves away from the lamina (Fig. 4a), compartments remain separated during the whole process of inversion. Consistently, microscopy shows that individual genomic loci reposition along with chromatin of their own compartment type during the entire process of nuclear inversion in rods *in vivo* (Extended Data Fig. 9). For example, the rhodopsin locus remains associated with euchromatin (A compartment) and the rhodopsin receptor remains expressed throughout the process of inversion (Fig. 4c).

To further test our proposed mechanism of compartmentalization, we initialized simulations from an inverted geometry and reintroduced lamina–heterochromatin interactions. These simulations predicted only partial de-inversion: whereas B monomers replaced A monomers at the periphery of the nucleus, C monomers remained as a single large globule surrounded by B monomers and associated with the lamina (Extended Data Fig. 10a). We tested these predictions experimentally by imaging de-differentiating rods of R7E mice²⁸ that express poly(Q)-expanded ataxin-7. Rods in these mice start lamin A/C expression after their nuclear inversion is completed²⁰ and acquire partially de-inverted morphologies that are remarkably similar to simulations (Extended Data Fig. 10b).

Together, our results show the central role of interactions between heterochromatin in establishing compartmentalization by phase separation. Using polymer simulations to reconcile microscopy and Hi-C data, we find that: (i) interactions between heterochromatic regions lead to phase separation of chromatin and these are essential for the compartmentalization of conventional and inverted nuclei; (ii) euchromatic interactions are dispensable for compartmentalization; and (iii) although lamina–heterochromatin interactions are dispensable for the segregation of euchromatin and heterochromatin, they are necessary to establish the conventional nuclear architecture. Although we narrow the search for key molecular determinants of compartmentalization to heterochromatin-associated molecules, making predictions for perturbations to particular molecular determinants

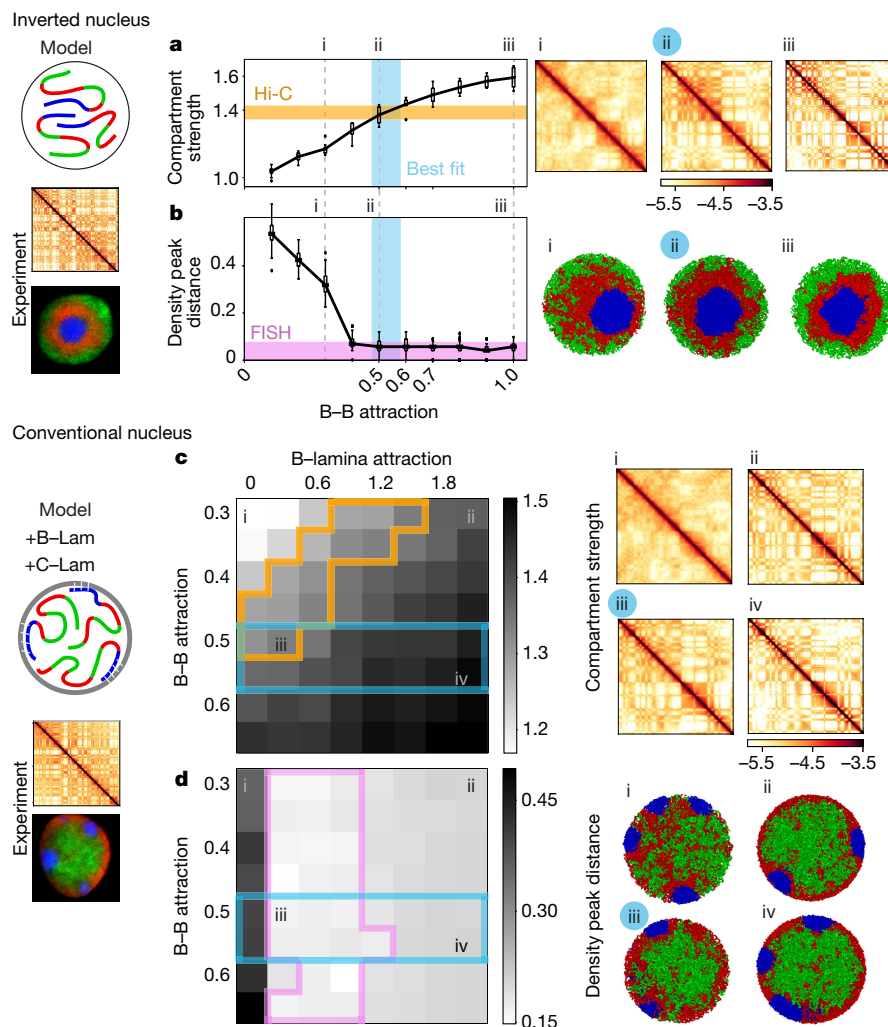


Fig. 3 | Heterochromatin-based mechanisms quantitatively reproduce inverted and conventional nuclei. **a, b,** Model for the inverted nucleus. Starting with the parameter ordering required to reproduce the morphology of the inverted nucleus (Fig. 2), we then varied B–B interactions to find models that best agree with Hi-C and microscopy data. **a**, Compartment strength as a function of B–B attraction (box plots as in Fig. 1c, with eight simulated chromosomes averaged across 150 conformations). Orange lane, compartment strength from rod Hi-C (see Fig. 1c). Blue, parameter range in agreement with Hi-C. Grey dashed lines, B–B values for which configurations and Hi-C maps are shown. **i–iii**, Simulated Hi-C maps ($\log_{10}(\text{contact frequency})$, chromosome 1: 50 Mb–150 Mb) are shown for indicated values of B–B. Model ii (highlighted) agrees best with Hi-C compartment strength. Attracting a small number of B monomers to the nuclear periphery does not disrupt the inverted architecture (Extended Data Fig. 7a). **b**, Distance between model and microscopy (as in Fig. 2b, c) as a function of B–B attraction (averaged over 150 conformations, box plots as in Fig. 1c). Purple lane, region of best agreement with microscopy (Methods); blue, as in **a**.

Representative conformations are shown to the right (i–iii). **c, d**, Model for the conventional nucleus. The model for conventional nuclei additionally includes interactions of monomers with the nuclear lamina. B monomers are attracted to the lamina with a strength B–Lam and C monomer clusters are pinned to the lamina at random positions. **c**, Compartment strength as a function of B–B and B–Lam attractions, calculated as in **a**. **i–iv**, Simulated Hi-C maps displayed for indicated parameters. Experimental compartment strength (orange outline, for conventional wild-type thymocytes) can be matched (iii) even if B–B interactions are constrained to be the same as for inverted nuclei (blue outline). **d**, Distance between microscopy and models (over 150 simulated conformations). **i–iv**, Representative conformations for indicated parameters. Agreement with microscopy (purple outline) and Hi-C (blue outline) is simultaneously achievable (iii, highlighted) with B–B attraction strength from the best inverted nucleus model. Attracting a small number of A monomers to the periphery, or tethering a fraction of chromocentres to the interior, does not alter our conclusions (Extended Data Fig. 7).

remains a limitation of our current study. Candidates for mediators of heterochromatin–heterochromatin interactions include affinity between homotypic repetitive elements^{1,9,29} or modified histones, and heterochromatin-associated proteins (for example, HP1)^{10,11}. Future work should consider the interplay between the mechanisms considered here and other chromosomal processes, such as non-equilibrium decondensation after mitosis³⁰ and loop extrusion⁸. Our results indicate that the inverted nucleus conceptually represents the default nuclear architecture imposed by the mechanism of compartmental interactions and that the conventional nucleus requires additional lamina–heterochromatin interactions. As most eukaryotic

nuclei have a conventional organization, our work raises questions about the functional relevance of heterochromatin positioning at the nuclear periphery.

Online content

Any methods, additional references, Nature Research reporting summaries, source data, statements of data availability and associated accession codes are available at <https://doi.org/10.1038/s41586-019-1275-3>.

Received: 11 January 2018; Accepted: 26 April 2019;
Published online 5 June 2019.

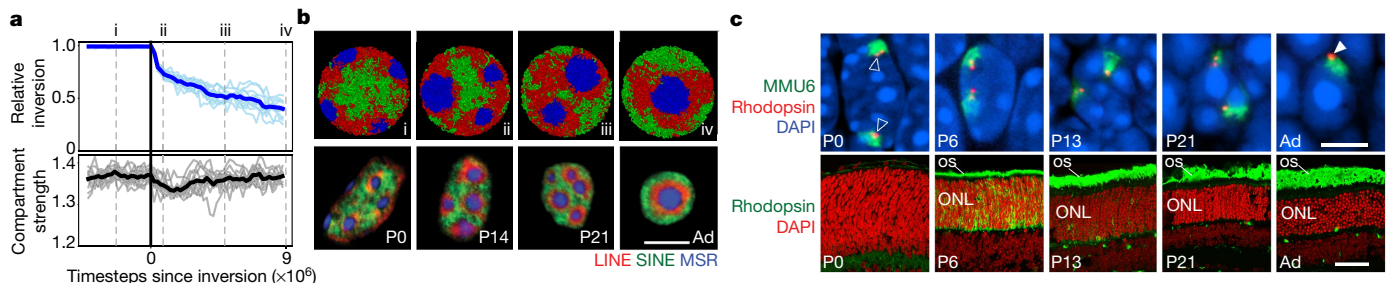


Fig. 4 | The time course and maintenance of compartment strength during nuclear inversion in the model and experiment. **a**, Simulated nuclear inversion. Configurations indicated by numerals and grey dashed lines are displayed in **b**. Black vertical line indicates the time at which interactions with the lamina are eliminated. Top, C monomers move towards the nuclear interior after removal of lamina interactions. Light-blue lines are computed from individual simulations; dark-blue line shows the average of the simulations. Bottom, compartment strength is maintained during inversion, showing only a transient dip. **b**, Representative conformations from simulations (top; see Extended Data Fig. 8a) mirror changes in chromatin architecture during rod differentiation *in vivo* at different developmental stages (postnatal day (P)0, P14, P21 and adult (Ad; 3.5 months); bottom) detected by FISH with probes for long interspersed nuclear elements (LINEs; L1, red),

short interspersed nuclear elements (SINES; B1, green) and major satellite repeats (MSRs; blue). The progression of geometries remains unchanged when simulated inversion is accompanied by volume decrease (Extended Data Fig. 8c), in accordance with *in vivo* observations¹⁹.

c, Top, in the process of nuclear inversion, the rhodopsin locus (red) within chromosome 6 (MMU6; green) changes position from internal (empty arrowheads) to peripheral (filled arrowhead) but remains within the A compartment (see Extended Data Fig. 9 for other genomic regions). Bottom, despite this marked relocation, rhodopsin gene expression, which starts at P6, continues at an increasing rate. OS, outer segments of rods positive for rhodopsin staining (green); ONL, outer nuclear layer containing rod perikarya. Single confocal sections (**b**, bottom) and projections of 2-μm confocal stacks (**c**). Scale bars, 5 μm (**b**, bottom and **c**, top) and 50 μm (**c**, bottom).

- Solovei, I., Thanisch, K. & Feodorova, Y. How to rule the nucleus: *divide et impera*. *Curr. Opin. Cell Biol.* **40**, 47–59 (2016).
- van Steensel, B. & Belmont, A. S. Lamina-associated domains: links with chromosome architecture, heterochromatin, and gene repression. *Cell* **169**, 780–791 (2017).
- Bonve, B. & Cavalli, G. Organization and function of the 3D genome. *Nat. Rev. Genet.* **17**, 661–678 (2016).
- Jerabek, H. & Heermann, D. W. How chromatin looping and nuclear envelope attachment affect genome organization in eukaryotic cell nuclei. *Int. Rev. Cell Mol. Biol.* **307**, 351–381 (2014).
- Jost, D., Carrivain, P., Cavalli, G. & Vaillant, C. Modeling epigenome folding: formation and dynamics of topologically associated chromatin domains. *Nucleic Acids Res.* **42**, 9553–9561 (2014).
- Lee, S. S., Tashiro, S., Awazu, A. & Kobayashi, R. A new application of the phase-field method for understanding the mechanisms of nuclear architecture reorganization. *J. Math. Biol.* **74**, 333–354 (2017).
- Di Pierro, M., Zhang, B., Aiden, E. L., Wolynes, P. G. & Onuchic, J. N. Transferable model for chromosome architecture. *Proc. Natl. Acad. Sci. USA* **113**, 12168–12173 (2016).
- Nuebler, J., Fudenberg, G., Imakaev, M., Abdennur, N. & Mirny, L. A. Chromatin organization by an interplay of loop extrusion and compartmental segregation. *Proc. Natl. Acad. Sci. USA* **115**, E6697–E6706 (2018).
- van de Werken, H. J. G. et al. Small chromosomal regions position themselves autonomously according to their chromatin class. *Genome Res.* **27**, 922–933 (2017).
- Larson, A. G. et al. Liquid droplet formation by HP1α suggests a role for phase separation in heterochromatin. *Nature* **547**, 236–240 (2017).
- Strom, A. R. et al. Phase separation drives heterochromatin domain formation. *Nature* **547**, 241–245 (2017).
- Machida, S. et al. Structural basis of heterochromatin formation by human HP1. *Mol. Cell* **69**, 385–397 (2018).
- Ganai, N., Sengupta, S. & Menon, G. I. Chromosome positioning from activity-based segregation. *Nucleic Acids Res.* **42**, 4145–4159 (2014).
- Grosberg, A. Y. & Joanny, J.-F. Nonequilibrium statistical mechanics of mixtures of particles in contact with different thermostats. *Phys. Rev. E* **92**, 032118 (2015).
- Smrek, J. & Kremer, K. Small activity differences drive phase separation in active-passive polymer mixtures. *Phys. Rev. Lett.* **118**, 098002 (2017).
- Stevens, T. J. et al. 3D structures of individual mammalian genomes studied by single-cell Hi-C. *Nature* **544**, 59–64 (2017).
- Hilbert, L. et al. Transcription organizes euchromatin similar to an active microemulsion. Preprint at <https://www.biorxiv.org/content/10.1101/234112v2> (2018).
- Zheng, X. et al. Lamins organize the global three-dimensional genome from the nuclear periphery. *Mol. Cell* **71**, 802–815 (2018).
- Solovei, I. et al. Nuclear architecture of rod photoreceptor cells adapts to vision in mammalian evolution. *Cell* **137**, 356–368 (2009).
- Solovei, I. et al. LBR and lamin A/C sequentially tether peripheral heterochromatin and inversely regulate differentiation. *Cell* **152**, 584–598 (2013).
- Eberhart, A. et al. Epigenetics of eu- and heterochromatin in inverted and conventional nuclei from mouse retina. *Chromosome Res.* **21**, 535–554 (2013).
- Tan, L., Xing, D., Chang, C.-H., Li, H. & Xie, X. S. Three-dimensional genome structures of single sensory neurons in mouse visual and olfactory systems. *Nat. Struct. Mol. Biol.* **26**, 297–307 (2019).
- Imakaev, M. et al. Iterative correction of Hi-C data reveals hallmarks of chromosome organization. *Nat. Methods* **9**, 999–1003 (2012).
- Ou, H. D. et al. ChromEMT: visualizing 3D chromatin structure and compaction in interphase and mitotic cells. *Science* **357**, eaag0025 (2017).
- Choo, K. H. A. *The Centromere* (Oxford Univ. Press, 1997).
- Rubinstein, M. & Colby, R. H. *Polymer Physics* (Oxford Univ. Press, 2003).
- Biggs, R., Liu, P. Z., Stephens, A. D. & Marko, J. F. Effects of altering histone posttranslational modifications on mitotic chromosome structure and mechanics. *Mol. Biol. Cell* **30**, 820–827 (2019).
- Helmlinger, D. et al. Glutamine-expanded ataxin-7 alters TFTC/STAGA recruitment and chromatin structure leading to photoreceptor dysfunction. *PLoS Biol.* **4**, e67 (2006).
- Tang, S.-J. Chromatin organization by repetitive elements (CORE): a genomic principle for the higher-order structure of chromosomes. *Genes* **2**, 502–515 (2011).
- Rosa, A. & Everaers, R. Structure and dynamics of interphase chromosomes. *PLOS Comput. Biol.* **4**, e1000153 (2008).

Acknowledgements We thank S. Bultrmann for help with rod cell sorting; A. S. Wang for help with sampling of *Lbr*^{-/-} thymus; D. Devys for samples of retinas from R7E mice; all members of the Mirny laboratory for many discussions; N. Abdennur for help with CTCF motif analysis; and N. Abdennur and P. Kerpedjiev for help with the HiGlass Hi-C browser. This work has been supported by NSF 1504942, NIH GM114190, NIH HG003143, NIH HG007743 and by the Deutsche Forschungsgemeinschaft grants SO1054/3 (I.S.) and SFB1064 (I.S. and H.L.). M.F. was supported by the Department of Defense through the National Defense Science & Engineering Graduate Fellowship (NDSEG) Program. J.D. and L.A.M. acknowledge support from the National Institutes of Health Common Fund 4D Nucleome Program (DK107980). J.D. is an investigator of the Howard Hughes Medical Institute.

Author contributions I.S., N.N., L.A.M. and J.D. conceived the project. Y.F. and I.S. obtained biological samples. N.N. performed Hi-C. M.F., M.I., G.F., B.R.L. and N.N. performed Hi-C analysis. M.F., with contributions from M.I., G.F. and L.A.M., performed simulations. Y.F., I.S. and B.J. conceived and performed microscopic experiments. M.F., Y.F. and I.S. prepared the figures. M.F., Y.F., G.F., I.S. and L.A.M. wrote the manuscript with contributions from N.N., M.I., H.L. and J.D.

Competing interests The authors declare no competing interests.

Additional information

Extended data is available for this paper at <https://doi.org/10.1038/s41586-019-1275-3>.

Supplementary information is available for this paper at <https://doi.org/10.1038/s41586-019-1275-3>.

Reprints and permissions information is available at <http://www.nature.com/reprints>.

Correspondence and requests for materials should be addressed to G.F., I.S. or L.A.M.

Publisher's note: Springer Nature remains neutral with regard to jurisdictional claims in published maps and institutional affiliations.

METHODS

Data reporting. No statistical methods were used to predetermine sample size. The experiments were not randomized and the investigators were not blinded to allocation during experiments and outcome assessment.

Cryosections and immunostaining. *Cryosections.* Retinas were sampled from CD1 mice at P0, P3, P6, P13, P21, P28 and at 3.5 months of age. Samples of retinas from R7E mice were provided by D. Devys. A detailed protocol of tissue fixation and cryosection preparation has been published previously³¹. In brief, tissues were fixed with 4% formaldehyde in PBS for 20–24 h, washed with PBS, incubated in solutions with increasing concentrations of sucrose (10%, 20% and 30%) and transferred into embedding moulds (Peel-A-Way Disposable Embedding Molds, Polysciences) filled with Jung freezing medium (Leica Microsystems). Tissue cryoblocks were frozen by immersing the moulds into a –80 °C ethanol bath, and stored at –80 °C. Cryosections with a thickness of 16–20 µm were cut using a Leica Cryostat (Leica Microsystems), collected on SuperFrost microscopic slides (SuperFrost Ultra Plus), immediately frozen and stored at –80 °C before use.

Immunostaining. Rhodopsin expression during rod differentiation was studied with antibodies against rhodopsin (RET-P1, Abcam). Nuclear architecture of retinal cells in degenerating retina of R7E mice was studied using antibodies against the euchromatin marker of histone modification, H3K9ac (donated by H. Kimura), ATAXN7 (provided by D. Devys) and lamin A/C (provided by H. Herrmann). Secondary antibodies were conjugated to Alexa 488, Alexa 555, Alexa 594 or Alexa 647 (Invitrogen). A detailed description of the immunostaining protocol has been published previously³². In brief, sections were incubated with primary and secondary antibodies diluted in blocking solution (1% BSA, 0.1% Triton X-100 and 0.1% saponin) under glass chambers for 18–20 h at room temperature. Washes (3 × 30 min) in between and after antibody incubations were performed with 0.05% Triton X-100 in PBS at 37 °C. For nuclear counterstaining, DAPI was added to the secondary antibody solution at a final concentration of 2 mg ml^{−1}.

FISH and microscopy. *FISH.* FISH on cryosections was performed according to the previously published protocol³¹. In brief, cryosections were dried for 30 min at room temperature, rehydrated in 10 mM sodium citrate buffer (pH 6.0) and heated in the same buffer for 30 min at 80 °C for antigen retrieval. After equilibration with 2 × SSC buffer and incubation with 50% formamide in 2 × SSC for 30 min, probes were loaded onto cryosections under small glass chambers, sealed with rubber cement and pre-incubated on a heating block at 45 °C for 1 h. Tissue and probe DNA were denatured simultaneously on a heating block at 80 °C for 3–5 min. Hybridization was carried out at 37 °C for 2 days. After hybridization, sections were washed with 2 × SSC at 37 °C and 0.1 × SSC at 61 °C, counterstained with 2 µg ml^{−1} DAPI for 1 h and mounted in Vectashield anti-fade medium (Vector Laboratories).

FISH probes. BAC clones used in the study were purchased from BACPAC Resources (Children's Hospital Oakland). For coordinates of all BACs, see Supplementary Table 2. BAC DNA was amplified from a miniprep using GenomiPhi kit (GE Healthcare, UK), labelled by nick translation with fluorescein-conjugated nucleotides and purified using QIAquick Nucleotide Removal Kit 50 (Qiagen). dUTPs were labelled with FITC, Cy3, Texas Red or Cy5 according to the published protocol³³. To verify BAC clones and exclude those that cross-hybridize to other chromosomes, all BAC probes were first labelled with digoxigenin-dUTP and co-hybridized with a respective chromosome paint labelled with biotin-dUTP to mouse metaphase spreads. Hybrids were detected with anti-digoxigenin antibody conjugated to FITC (Jackson Immuno Research) and avidin conjugated to Alexa 555 (Invitrogen Molecular Probes). Mouse chromosome paints were a gift from J. Wienberg. The paints were first amplified and then labelled with biotin-dUTP or Cy3-dUTP by degenerate oligonucleotide-primed polymerase chain reaction (DOP-PCR) using 6MW primer (5'-CCGACTCGAGNNNNNNATGTGG-3', Eurogentec). For FISH probe preparation, 4 µg of labelled BAC or 6 µg of chromosome paint, were mixed with 10 µg of salmon sperm DNA and 50 µg of mouse Cot-1 DNA, ethanol-precipitated and dissolved in 10 µl of hybridization mixture consisting of 50% deionized formamide (Sigma-Aldrich), 10% dextran sulphate (Amersham Biosciences) and 1 × SSC³¹. Probes for FISH with SINEs (B1) and LINEs (LINE1) and major satellite repeats are described in a previous study¹⁹.

Immuno-FISH. For the nuclear lamina staining after FISH, sections were equilibrated in PBS and stained as described above using antibodies against lamin B1 (Santa Cruz, sc-6217) or lamin A/C and LBR (both provided by H. Herrmann).

Microscopy and image analysis. Image stacks were acquired using a Leica TCS SP5 confocal microscope equipped with Plan Apo 63×/1.4 NA oil-immersion objective and lasers for blue (405 nm), green (488 nm), orange (561 nm), red (594 nm) and far-red (633 nm) fluorescence. Multichannel image stacks were corrected for chromatic shift and processed using a dedicated ImageJ plugin 'Stack Groom'³⁴.

Mice. Mice used for tissue sampling were obtained from Charles River Laboratories, housed at the Biocentre, Ludwig Maximilians University of Munich (LMU) and treated according to the standard protocol approved by the Animal Ethics Committee of LMU.

Tissue sampling for Hi-C. Retinas from CD1 and C3H adult mice (retired breeders) were dissociated into a single-cell suspension using the Papain Dissociation System (Worthington Biochemical Corporation) as described elsewhere³⁵. Four retinas from two mice were used for one biological replica. To obtain a pure population of rod photoreceptors, retina suspensions were sorted based on standard forward and sideward scatter settings using FACS Aria II (Becton Dickinson) and yielded about 1 million rod perikarya (Supplementary Fig. 1). Retinas of C3H mice, which lack the entire outer nuclear layer, were used to obtain the non-rod population of retinal neurons. Each biological replica of non-rod neurons contained approximately 10 million cells. Thymocytes from wild-type CD1 mice and *Lbr*^{−/−} mice³⁶ were extracted from thymi of young adult animals at P26 and P28, respectively. Thymi were minced, small tissue pieces were gently pipetted and the resulting single-cell suspension was pressed through a Cell Strainer Snap Cap with a mesh size of 35 µm. Each biological replica of thymocytes contained 25 million–30 million cells. Images of microscopic controls of isolated rods, non-rod neurons and thymocytes are shown in Supplementary Fig. 1. All cells were fixed with 1% formaldehyde (Fisher Scientific, 10532955) for 10 min at room temperature. Fixation was quenched with 0.1 M glycine for 5 min at room temperature and then for 15 min at 4 °C. Fixed cells were pelleted, snap-frozen and kept at –80 °C until use.

Hi-C. Hi-C was performed as described previously³⁷ with modifications.

Cell lysis and chromatin digestion. In brief, 450,000 formaldehyde-cross-linked rod nuclei and up to 5 million of other cell types were incubated in 1 ml of cold lysis buffer (1 ml 10 mM Tris-HCl pH 8.0, 10 mM NaCl, 0.2% (v/v) Igepal CA630, mixed with 100 µl protease inhibitors (Sigma P8340) immediately before use) on ice for 15–20 min. Next, samples were lysed with a Dounce homogenizer and pestle A (KIMBLE Kontes, 885303-0002) by moving the pestle slowly up and down 25 times, incubating on ice for 1 min followed by 10 more strokes with the pestle. The suspension was centrifuged for 5 min at 9,800 r.p.m. (rod nuclei) and 4,500 r.p.m. (all other samples) at room temperature using a table-top centrifuge (Centrifuge 5810R, Eppendorf). The supernatant was carefully removed from the sample containing rod nuclei and spun a second time (9,800 r.p.m., 5 min) and then both pellets were combined. Pellets were washed twice with ice-cold 500 µl 1 × NEBuffer 2 (NEB). After the second wash, each pellet was resuspended in 1 × NEBuffer 2 in a total volume of 352 µl, chromatin was solubilized by addition of 38 µl 1% SDS per tube, the mixture was resuspended and incubated at 65 °C for 10 min. Tubes were placed on ice and 44 µl of 10% Triton X-100 was added. Chromatin was subsequently digested by adding 400 units HindIII (NEB) at 37 °C for 15 h with continuous slow rocking in parafilm-sealed tubes. Digested chromatin solutions were spun shortly, transferred to ice and used for generating Hi-C libraries.

Biotin marking of DNA ends and blunt-end ligation. The HindIII DNA ends were filled in and marked with biotin by adding 70 µl fill-in mix (2 µl 10 mM dATP, 2 µl 10 mM dGTP, 2 µl 10 mM dTTP, 42 µl 0.4 mM biotin-14-dCTP (Invitrogen 19518-018), 7 µl 10 × NEBuffer 2 and 15 µl 5 µl^{−1} Klenow polymerase (NEB M0210L)) followed by incubation at 37 °C for 4 h on a rocking platform at 50 r.p.m. Klenow polymerase was inactivated by adding 96 µl 10% SDS followed by incubation at 65 °C for 30 min. Tubes were then immediately placed on ice; the content of each of the tube was transferred to a 15-ml conical tube containing 7.58 ml ligation mix (820 µl 10% Triton X-100, 758 µl 10 × ligation buffer (500 mM Tris-HCl pH 7.5, 100 mM MgCl₂ and 100 mM DTT), 82 µl 10 mg ml^{−1} BSA, 82 µl 100 mM ATP and 5.84 ml water). Subsequently, 50 µl 1 U µl^{−1} T4 DNA ligase (Invitrogen, 15224) was added and mixed by inverting tubes; ligation was performed at 16 °C overnight. For DNA purification, 50 µl of 10 mg ml^{−1} proteinase K (Invitrogen, 25530-031) was added to each tube and samples were incubated at 65 °C for 4 h followed by a second addition of 50 µl of 10 mg ml^{−1} proteinase K solution and 8 h incubation at 65 °C. Tubes were cooled to room temperature and DNA samples were transferred to 50-ml conical tubes. The DNA was extracted by adding an equal volume of phenol pH 8.0 (Fisher, BP1750I-400), vortexing for 3 min and spinning for 10 min at 4,000 r.p.m. in a table-top centrifuge (centrifuge 5810R, Eppendorf). The supernatants were transferred to new 50-ml conical tubes. Another two extractions were performed with an equal volume of phenol, pH 8.0:chloroform (1:1). Next, supernatants with Hi-C libraries were concentrated and desalting on 30-kDa Amicon Ultra 15-ml columns (Fisher Scientific, UFC903024) by spinning once for 10 min at 4,000 r.p.m. in a table-top centrifuge (centrifuge 5810R, Eppendorf). The flow-through was discarded and each column was washed once with 5 ml milliQ water. Then, samples were dissolved in 1 ml 1 × TE buffer, transferred to 30-kDa Amicon Ultra 0.5-ml columns (Fisher, UFC5030BK) and spun at 10,000 r.p.m. in a microcentrifuge. The flow-through was discarded. Columns were washed twice with 450 µl TE. After the final wash, the Hi-C library was dissolved in 100 µl water. Aliquots of Hi-C libraries were run on a gel to estimate the amount of DNA in the samples: 5 µl of rod Hi-C libraries and 2 µl for all other libraries.

Biotin removal from unligated ends. Hi-C libraries were treated with T4 DNA polymerase to remove biotinylated ends that did not ligate (dangling ends).

The reactions were assembled as follows: Hi-C library (up to 5 µg DNA), 1.3 µl 10 mg ml⁻¹ BSA, 13 µl 10 × NEBuffer 2, 0.325 µl 10 mM dATP, 0.325 µl 10 mM dGTP and 30 units T4 DNA polymerase (NEB, M0203L) in a total volume of 130 µl. Reactions were mixed in a single tube, split between wells on a PCR plate and incubated at 20 °C for 5 h. Samples were pooled and the reaction was stopped by addition of 5.2 µl 0.5 M EDTA pH 8.0.

DNA fragmentation. The DNA was sheared to a size of 100–400 bp (with the majority of molecules around 200 bp) using a Covaris S2 instrument (Covaris). The settings were as follows: duty cycle 10%, intensity 5, cycles per burst 200, set mode frequency sweeping, process time 60 s per process, cycle number 3. DNA size was checked by running an aliquot on a 2.5% agarose gel and samples were sonicated for an additional half-cycle when deemed necessary, which allowed us to avoid library size selection. The DNA samples were purified using DNA MinElute columns (Qiagen, 5 µg DNA per column) and PB buffer (Qiagen). Elution was done in two steps with hot (65 °C) EB buffer so that the total volume of each Hi-C library was about 70 µl. DNA amounts were estimated to 5–9 µg of DNA per library by running aliquots on 2.5% agarose gel along with 100 ng of a low molecular weight DNA ladder (NEB, N3233L).

End repair and 'A' tailing. A single DNA end-repair reaction per Hi-C library was performed by adding 10 µl 10 × ligation buffer (NEB, B0202S), 1.6 µl 25 mM dNTP mix, 5 µl T4 DNA polymerase (3 U µl⁻¹, NEB, M0203L), 5 µl T4 polynucleotide kinase (10 U µl⁻¹, NEB, M0210S), 1 µl Klenow DNA polymerase (5 U µl⁻¹, NEB, M0210S) and water up to 100 µl. The reaction was incubated at 20 °C for 1 h followed by purification of the DNA with a Qiagen MinElute column (Qiagen, up to 5 µg DNA per column). The DNA was eluted twice with 25 µl hot EB buffer (Qiagen). The eluates for each single column were pooled. Next, A-tailing reactions that adenylate the 3' ends of the fragments were carried out by incubation with 7.5 µl 10 × NEBuffer 2, 15 µl 1 mM dATP, 4.5 µl Klenow (exo-) (NEB, M0212L) and water to 75 µl. The reaction was incubated at 37 °C for 1 h followed by incubation at 65 °C for 20 min to inactivate the Klenow polymerase. The reactions were cooled on ice, all tubes for a library were pooled and the volume adjusted to 200 µl with 1 × TLE buffer (10 mM Tris pH 8.0, 0.1 mM EDTA).

Streptavidin pull-down of biotinylated Hi-C ligation products. All subsequent steps were performed in DNA LoBind tubes (Eppendorf, 22431021) and each step was performed in a fresh tube. Then, 100 µl of streptavidin Dynabeads (MyOne Streptavidin C1 Beads, Invitrogen, 650-01) were washed twice with 400 µl Tween wash buffer (5 mM Tris-HCl pH 8.0, 0.5 mM EDTA, 1 M NaCl, 0.05% Tween-20) by incubating for 3 min at room temperature with rotation, reclaiming against a magnetic separation rack (Genscript, M00140) for 1 min and removing all supernatant. Next, reclaimed beads were resuspended in 200 µl 2 × binding buffer (10 mM Tris-HCl pH 8.0, 1 mM EDTA, 2 M NaCl) and combined with 200 µl Hi-C DNA from the previous step. The mixture was incubated at room temperature for 30 min with rotation. The supernatant was removed and the DNA-bound streptavidin beads were washed once with 400 µl 1 × binding buffer. The beads were then washed with 100 µl 1 × ligation buffer (Invitrogen, 5 × buffer) with extra ATP (4 µM final concentration), and then resuspended in 38.8 µl 1 × ligation buffer.

Paired-end adaptor ligation. Ligation reactions were prepared as follows: 38.8 µl Hi-C library on beads, 6 µl Illumina paired-end adapters (Illumina), 2.25 µl 5 × ligation buffer (Invitrogen, supplied with T4 DNA ligase), 3 µl T4 DNA ligase (Invitrogen, 15224). The reaction was incubated at room temperature for 5 h. The beads with bound ligated Hi-C DNA were collected by holding the tubes against a magnetic separation rack (Genscript, M00140), washed twice with 400 µl 1 × Tween wash buffer for 5 min on a rocking platform, once with 200 µl 1 × binding buffer, twice with 200 µl 1 × NEBuffer 2 to remove non-ligated paired-end adapters and resuspended in 18 µl 1 × NEBuffer 2.

Library amplification. Six PCR reactions per library were set up, each containing 3 µl Dynabead-bound Hi-C library, Illumina PE1.0 and PE2.0 PCR primers (0.7 µl each; corresponding to 17.5 pmol each), 0.4 µl 25 mM dNTPs, 1 µl Pfu Ultra II Fusion DNA polymerase (Stratagene, 600670), 5 µl 10 × Pfu Ultra buffer and 39.2 µl water. The temperature profile during the PCR amplification was 30 s at 98 °C followed by nine cycles of 10 s at 98 °C, 45 s at 65 °C, 30 s at 72 °C and a final 7-min extension at 72 °C. The PCR reactions were pulled together, streptavidin beads were collected using a magnetic separation rack for 2 min and supernatants were transferred to new tubes. Hi-C libraries were purified from the supernatants using Ampure XP beads (Becman Coulter, A63881) as follows: 1.8 × volumes of the beads were added to Hi-C samples, briefly vortexed, incubated at room temperature for 10 min and then collected using a magnetic rack for 5 min. Supernatants were discarded and beads were washed twice with 1 ml freshly made 70% ethanol. Air-dried beads were resuspended in 35 µl TLE buffer, incubated at room temperature for 15 min while tapping the tubes every 1–2 min and collected using a magnetic rack for 5 min. Supernatants were transferred to fresh tubes. The quality of Hi-C libraries was confirmed by NheI restriction digest of 8 µl of each Hi-C library. Digested samples were run in parallel with undigested samples on a 2% agarose gel. More than 50% of each Hi-C library was digested,

and all libraries were qualified for sequencing on an Illumina GAII paired-end sequencing platform.

Data analysis for Hi-C. *Hi-C data processing.* We mapped our reads to the mm9 genome assembly, and subsequently filtered and corrected the reads using ICE as described previously²³. We removed bins with less than half of the bin sequenced, in addition to bins at the lowest 1% of coverage. We truncated the top 0.05% of *trans* contacts, which were probably PCR blowouts. Read statistics can be found in Supplementary Table 1, with a comparison to other primary tissue datasets.

Compartment profile. In order to define compartment strength, it is necessary to have a particular assignment of Hi-C bins to compartments. For simulations, we know the sequence of A and B monomers along our simulated chromosomes. Hence, we can make the choice that a bin in our simulated Hi-C map is an A- or B-compartment bin if the majority of monomers belonging to that bin are A or B monomers. For experimental data, the process is more involved. For each chromosome, we take the *cis*-contact map, and following iterative correction and removal of distance decay to produce an 'observed over expected' matrix²³, we compute eigenvectors of the mean-centred observed-over-expected matrix. The eigenvector with the largest magnitude eigenvalue is the 'compartment signal'. However, the mathematics of this operation leaves the sign of the eigenvector ambiguous, although the partitioning of the genome into two separate compartments suggests it is not. The established convention is that the sign of this eigenvector is chosen such that the compartment signal correlates positively with GC content²³ or density of transcription start sites³⁸. In this convention, B-compartment bins are those for which the compartment signal is negative, and A compartment bins are those for which the compartment signal is positive.

Saddle plots. For each chromosome, we sort the compartment eigenvector from the lowest to the highest value. We then reshuffle the observed-over-expected map of the chromosome according to this ordering. We coarse-grain the resulting map into a 50-by-50 matrix, where the element (i, j) is the average value in the reshuffled map between bins of the i th 50-cile and the j th 50-cile. The saddle plot is the average of these coarse-grained maps over all chromosomes in both replicates. Analysis was performed at a resolution of 50 kb per bin.

Compartment strength. Given an assignment of bins to compartments, we define compartment strength first on a per-bin level. The compartment strength of bin i (CS_i) is the average number of contacts it makes with other bins of the same compartment type in the observed-over-expected heat map, divided by the average number of contacts it makes with any bin in the observed-over-expected heat map. The compartment strength of the total data set is then $\langle CS_i \rangle$, where the average is taken over all bins, weighted equally. Note that this metric is independent of the orientation of the compartment profile, since the two compartments are treated symmetrically. If there is no compartmentalization, the metric is 1, whereas any pattern of compartmentalization yields a compartment strength greater than 1.

TAD strength. Two methods were used to analyse TAD strength. First, on the basis of the calls from a previous study³⁹, each TAD was rescaled such that it was a 30-by-30 bin heat map, and averaged together with other TADs within the same chromosome (Extended Data Fig. 3b). For each of these rescaled TADs, we computed their observed-over-expected maps, and compared the sum of their corners to the average of the two triangles adjacent to the corner. The side of each triangle was 12 bins. This is illustrated in the schematic shown in Extended Data Fig. 3b. TAD strength was then computed as the average of these values.

Second, TADs were called using corner score, implemented in the package lavaburst (<https://github.com/nvictus/lavaburst>) with default parameters (Extended Data Fig. 3f). Average enrichments of TADs were then calculated as described previously⁴⁰. For each TAD call, we took a matrix that was three times the size of a TAD, with a TAD located in the centre of the matrix. The matrix was then rescaled to a 90 × 90 matrix, with the TAD occupying the central (30:60, 30:60) square. The average TAD was obtained by averaging these 90 × 90 matrices. TAD strength was also calculated similarly to a previous study⁴⁰. It was defined as a ratio (2 × within TAD)/(between TAD), where 'within TAD' is the sum of counts inside the TAD (30:60, 30:60) in the rescaled 90 × 90 matrix. 'Between TAD' is a sum of the counts between the TAD, and the regions before and after of the same length: (0:30, 30:60) and (30:60, 60:90) in the 90 × 90 matrix.

Insulation profiles. Insulation profiles are calculated following a previously published method⁴¹, removing two diagonals from each side of the main diagonal. Loci within two bins of a bad bin were also excluded. A window of size 200 kb was used with data at a resolution of 20 kb.

cis contact fraction. To quantify the territoriality of our data, we divided the number of *cis* (same chromosome, greater than 20 kb apart) reads by the sum of *cis* and *trans* (different chromosome) reads.

P(s) curves. The decay of contact probability as a function of distance from the diagonal is computed at the fragment level. *P(s)* curves were normalized such that they cross at 1 Mb.

Simulations. We perform Langevin dynamics of our coarse-grained model using a laboratory-developed wrapper for OpenMM^{42,43}, a high-performance

GPU-assisted MD API. Our chromosomes are constructed from equally sized spherical monomers with diameters defined to be of unit length. A rough estimate for how many base pairs each monomer represents is based on the identification of each polymer with one mouse chromosome.

Our simulations represent multiple copies of mouse chromosomes 1 and 2. The first 1,000 monomers proximal to the centromere region of each chromosome were assigned to be C monomers. The subsequent 5,000 monomers were A and B monomers mimicking the assignment of compartments in chromosome 1. We digitized the compartment eigenvector of chromosome 1, binned at 200 kb, and assigned five monomers to each of the first 1,000 bins to be A or B monomers if the corresponding eigenvector value was positive or negative, respectively. Chromosome 2 was represented similarly in simulations, but starting with the eigenvector of chromosome 2. To improve averaging of simulation observable values, our full system consisted of four copies of the chromosome 1- and four copies of the chromosome 2-derived sequences. Each monomer therefore represents 40 kb.

Unless otherwise noted, polymers were initialized as random walks. Preliminary simulations to determine orderings of parameter strengths were run for 2×10^6 time steps. Conventional parameter sweep simulations were run for 1.1×10^7 time steps and inverted parameter sweep simulations were run for 2.1×10^7 time steps, to allow for equilibration of compartment strength. Inversion simulations were initialized as the final configurations of conventional nuclei simulations, and were run for 0.9×10^7 time steps, with removal of the lamina occurring a quarter of the way through, after 2.25×10^6 time steps. Simulations of alternative models were run for 4.5×10^6 time steps, and de-inversion simulations were run for 2×10^7 .

We used six different energies in our equilibrium simulations: a stretching energy between pairs of adjacent monomers, a harmonic bending energy for triplets of monomers, spherical confinement, short-range attraction of B and C monomers to the lamina, a short-range inter-monomer attraction of varying strength, and a pinning of C monomers to the lamina. Details and functional forms can be found in Supplementary Information 1.

Simulated Hi-C heat maps were generated by counting contacts between pairs of loci over multiple simulation snapshots from multiple simulations. A contact was registered if the centres of two monomers were closer than 2.5 monomer diameters. For both the inverted and conventional model parameter sweeps, each data point represented contacts from the final 125 configurations of three separate simulations, with each configuration separated by 3,000 time steps. For enrichments over the inversion process, each data point was calculated from contacts obtained from 60 configurations drawn from eight separate simulations. For comparisons with Hi-C, after tallying contacts for the full simulation, any corresponding contacts that respond to contacts with C monomers were removed, as those represent regions that are not assayed in Hi-C due to low mappability. The resulting simulated Hi-C heat maps were then iteratively corrected and compartment strengths were computed in the same way as for experimental data.

For particular points in parameter space for which we wanted to display simulated Hi-C maps (Fig. 3b, e), 250 configurations from 50 simulations (for a total of 12,500 configurations) were necessary to smoothly sample the entire map.

Simulated configurations were compared quantitatively to microscopy through the distributions of each monomer type as a function of nuclear radius. For each monomer, we calculated its radial distance, normalized by the radius of the nucleus, and then binned according to the binning used previously¹⁹. Thus, for any configuration or group of configurations, we produced three distributions of monomer density as a function of nuclear radius, one for each of the three monomer types. For each distribution calculated in this way, we identified the radial distance at which the distribution achieved its maximum. We then computed the Euclidean distance between the peaks of our models and the peaks of the density functions described previously¹⁹, to quantitatively compare the performance of our models with respect to microscopy data. In figures, we refer to this metric as the density peak distance.

To ensure that our results are not sensitive to the choice of metric, we compare our density peak distance to two other measures of probability distribution function distance (Supplementary Fig. 4). These include Kullback–Leibler divergence (with reference distribution being the experimentally determined distribution), and the L^2 norm of the difference between the two distributions. Specifically, for each model class, and each monomer type, we compute the radial distributions, and then concatenate the three monomer-type distributions together. These are then compared (either with the L^2 norm or Kullback–Leibler divergence) to the similarly concatenated experimentally determined distribution. Good agreement with experiment was defined as being below the minimum value of density peak distance achieved in the parameter sweep plus $1.6 \times \text{s.d.}$ at that minimum value point.

Various geometrical aspects of the inversion process were also quantified. In Fig. 4, we track the average distance of the chromocentres from the nuclear centre, and normalize by the radius of the nucleus. In Extended Data Fig. 8, we track the average pairwise distance of all the chromocentres, normalized by the maximum pairwise distance. In both figures, we show the individual traces, computed from just one configuration, and then the average of the traces over 10 replicate

simulations. For Extended Data Fig. 8c, we increased the density from 0.15 to 0.55 in increments of 0.02, restarting our simulation every 225,000 time steps.

Choosing parameters for model-space exploration. To explore the six-dimensional space of our copolymer framework, we selected six energies and permuted them in terms of their assignments to the six possible attractions (Fig. 2a). The energies we chose were 0.02, 0.10, 0.20, 0.26, 0.34, and 0.44 (in units of kT). We selected these values such that for a sequence $XX, XY, YY:XY < (XX + YY)/2$, thereby satisfying the Flory–Huggins criterion for demixing of XX and YY. Thus, we expect that for any model class (which we define as a particular ordering of the attractions) the phase separation between XX and YY can take place.

Reporting summary. Further information on research design is available in the Nature Research Reporting Summary linked to this paper.

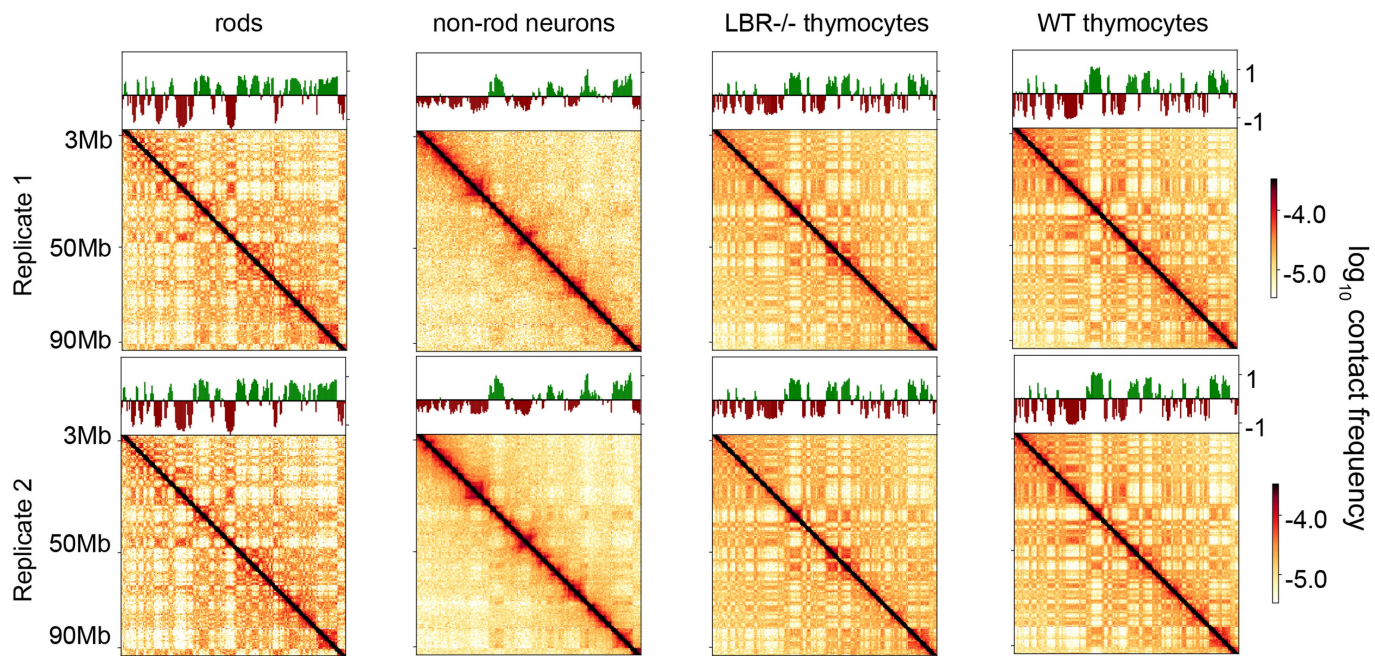
Data availability

Hi-C maps are available from the HiGlass browser (<http://mirnylab.mit.edu/projects/invnuclei/>) and from a public server (<http://higlass.io/app/?config=JLOHiPILTMq6qDRicHMJqg>). Hi-C maps are also available from the Gene Expression Omnibus (GEO) repository, accession number GSE111032.

Code availability

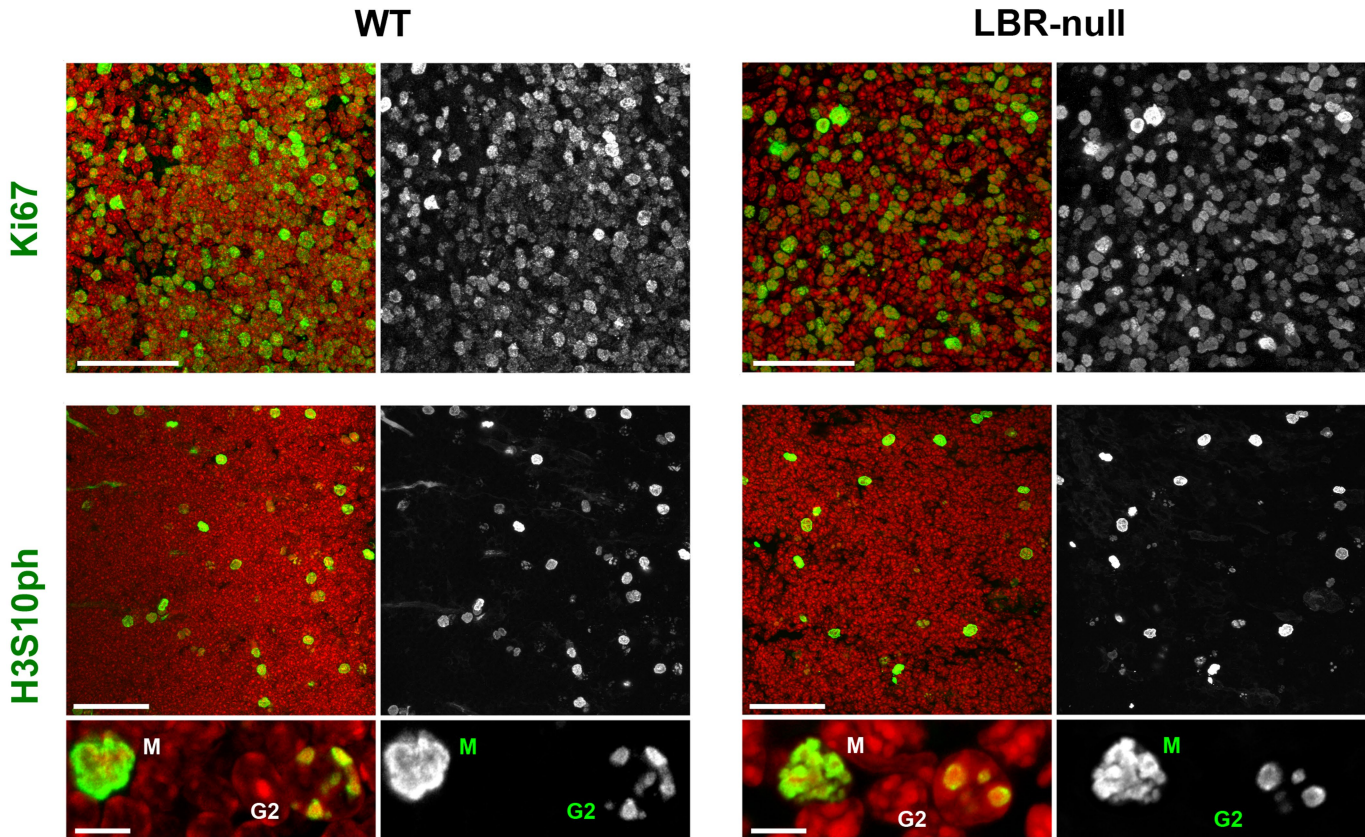
Software used to store and analyse Hi-C data can be accessed at <https://bitbucket.org/mirnylab/hiclib> and <https://bitbucket.org/mirnylab/mirnylib>. Data were also stored using the Cooler⁴⁴ software (<https://github.com/mirnylab/cooler>).

31. Solovei, I. Fluorescence in situ hybridization (FISH) on tissue cryosections. in *Methods Mol. Biol.* **659**, 71–82 (2010).
32. Eberhart, A., Kimura, H., Leonhardt, H., Joffe, B. & Solovei, I. Reliable detection of epigenetic histone marks and nuclear proteins in tissue cryosections. *Chromosome Res.* **20**, 849–858 (2012).
33. Cremer, M. et al. Multicolor 3D fluorescence in situ hybridization for imaging interphase chromosomes. *Methods Mol. Biol.* **463**, 205–239 (2018).
34. Walter, J. et al. Towards many colors in FISH on 3D-preserved interphase nuclei. *Cytogenet. Genome Res.* **114**, 367–378 (2006).
35. Feodorova, Y., Koch, M., Bultman, S., Michalakis, S. & Solovei, I. Quick and reliable method for retina dissociation and separation of rod photoreceptor perikarya from adult mice. *Methods Y* **2**, 39–46 (2015).
36. Cohen, T. V. et al. The lamin B receptor under transcriptional control of C/EBP ϵ is required for morphological but not functional maturation of neutrophils. *Hum. Mol. Genet.* **17**, 2921–2933 (2008).
37. Naumova, N. et al. Organization of the mitotic chromosome. *Science* **342**, 948–953 (2013).
38. Heinz, S. et al. Simple combinations of lineage-determining transcription factors prime *cis*-regulatory elements required for macrophage and B cell identities. *Mol. Cell* **38**, 576–589 (2010).
39. Nora, E. P. et al. Targeted degradation of CTCF decouples local insulation of chromosome domains from genomic compartmentalization. *Cell* **169**, 930–944 (2017).
40. Flyamer, I. M. et al. Single-nucleus Hi-C reveals unique chromatin reorganization at oocyte-to-zygote transition. *Nature* **544**, 110–114 (2017).
41. Crane, E. et al. Condensin-driven remodelling of X chromosome topology during dosage compensation. *Nature* **523**, 240–244 (2015).
42. Eastman, P. et al. OpenMM 4: a reusable, extensible, hardware independent library for high performance molecular simulation. *J. Chem. Theory Comput.* **9**, 461–469 (2013).
43. Eastman, P. et al. OpenMM 7: rapid development of high performance algorithms for molecular dynamics. *PLOS Comput. Biol.* **13**, e1005659 (2017).
44. Abdennur, N. & Mirny, L. Cooler: scalable storage for Hi-C data and other genetically-labeled arrays. Preprint at <https://www.biorxiv.org/content/10.1101/557660v1> (2019).
45. Shultz, L. D. et al. Mutations at the mouse ichthyosis locus are within the lamin B receptor gene: a single gene model for human Pelger–Huët anomaly. *Hum. Mol. Genet.* **12**, 61–69 (2003).
46. Dixon, J. R. et al. Topological domains in mammalian genomes identified by analysis of chromatin interactions. *Nature* **485**, 376–380 (2012).
47. Rao, S. S. P. et al. A 3D map of the human genome at kilobase resolution reveals principles of chromatin looping. *Cell* **159**, 1665–1680 (2014).
48. Schwarzer, W. et al. Two independent modes of chromatin organization revealed by cohesin removal. *Nature* **551**, 51–56 (2017).
49. Grant, C. E., Bailey, T. L. & Noble, W. S. FIMO: scanning for occurrences of a given motif. *Bioinformatics* **27**, 1017–1018 (2011).
50. Schmidt, D. et al. Waves of retrotransposon expansion remodel genome organization and CTCF binding in multiple mammalian lineages. *Cell* **148**, 335–348 (2012).
51. Kerpedjiev, P. et al. HiGlass: web-based visual exploration and analysis of genome interaction maps. *Genome Biol.* **19**, 125 (2018).
52. Zhang, Y. et al. Spatial organization of the mouse genome and its role in recurrent chromosomal translocations. *Cell* **148**, 908–921 (2012).
53. Lin, Y. C. et al. Global changes in the nuclear positioning of genes and intra- and interdomain genomic interactions that orchestrate B cell fate. *Nat. Immunol.* **13**, 1196–1204 (2012).
54. Kizilyaprak, C., Spehner, D., Devys, D. & Schultz, P. In vivo chromatin organization of mouse rod photoreceptors correlates with histone modifications. *PLoS ONE* **5**, e11039 (2010).



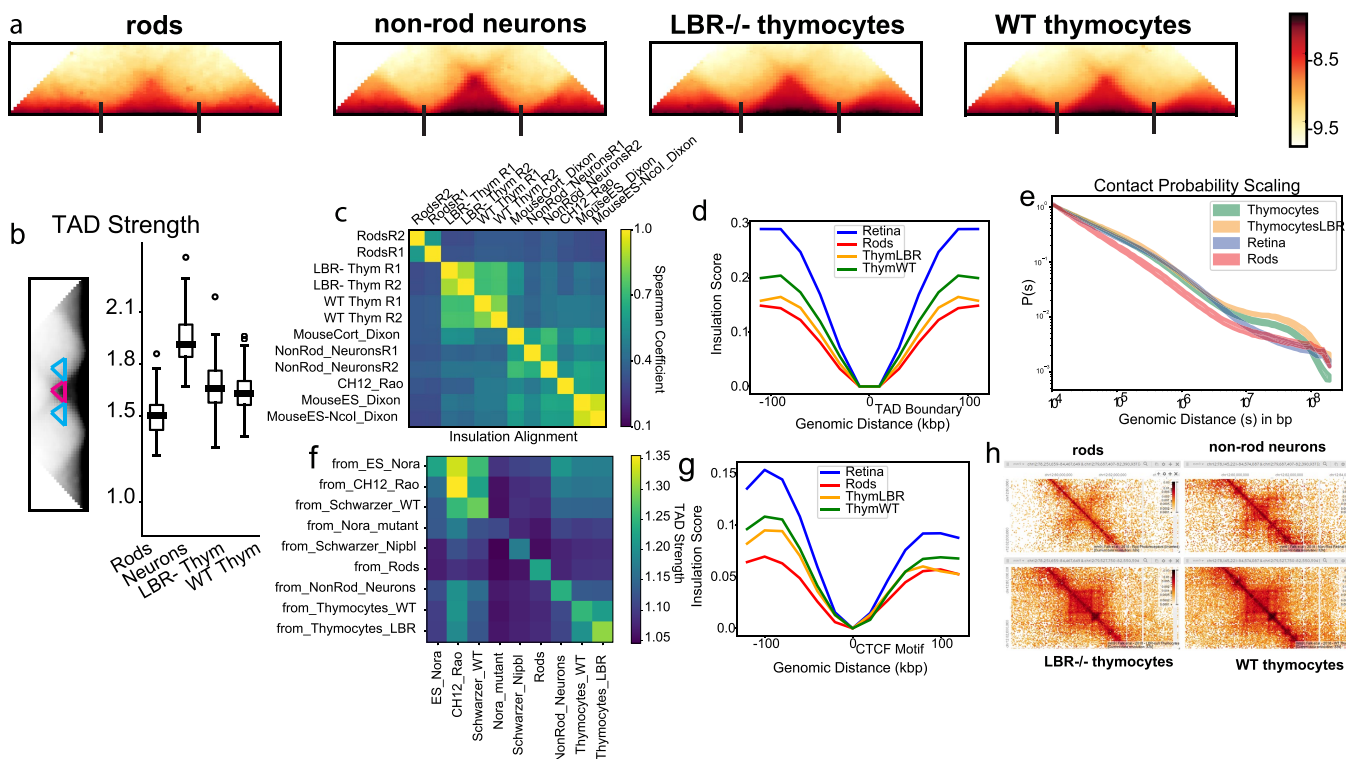
Extended Data Fig. 1 | Hi-C replicates show reproducible features. Hi-C maps are qualitatively similar between replicates. Hi-C maps (plotted as \log_{10} (contact frequencies)) for an 87-Mb region of chromosome 1. Compartment profiles indicating regions in the A (green) and B

(red-brown) compartments are shown above the Hi-C maps. Full maps are available to browse on the HiGlass website (<http://higlass.io/app/?config=JLOhiPILTmq6qDRicHMJqg>). For quantitative comparisons, see Extended Data Figs. 3, 4, 5.



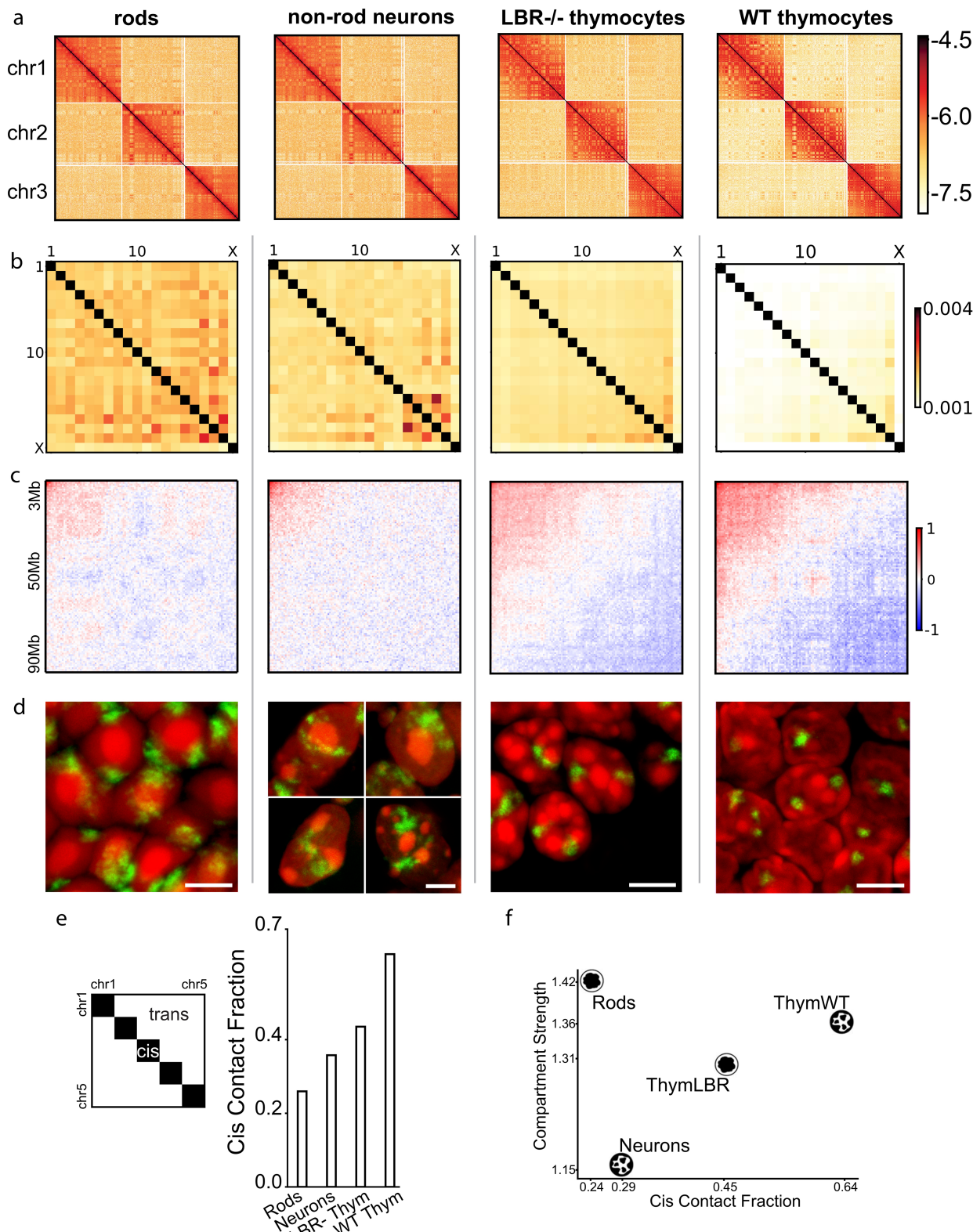
Extended Data Fig. 2 | The majority of thymocytes are actively cycling cells in both wild-type and *Lbr*^{-/-} mice. Left, wild-type mice; right, *Lbr*^{-/-} mice. Thymus cryosections were immunostained with antibodies for Ki-67, a marker of cycling cells, and phosphorylated histone H3 S10 (H3S10ph), a marker for G2 and mitotic cells. In agreement with the idea that *Lbr*^{-/-} mice have a seemingly normal immune system⁴⁵, the number of cycling thymocytes in thymi of *Lbr*^{-/-} mice is comparable to

that of wild-type mice. M, mitotic cells; G2, cells in mid/late G2. Ki-67 staining is shown as projections of 5-μm confocal stacks. Phosphorylated H3 S10 staining is shown as projections of 10-μm (for overviews) or 3-μm (for magnified areas) confocal stacks. Antibodies: mouse anti-phosphorylated H3 S10 (Abcam, ab14955) and rabbit anti-Ki-67 (Abcam, ab15580). Immunostaining and microscopy were performed as described in the Methods. Scale bars, 50 μm (top and middle) and 5 μm (bottom).



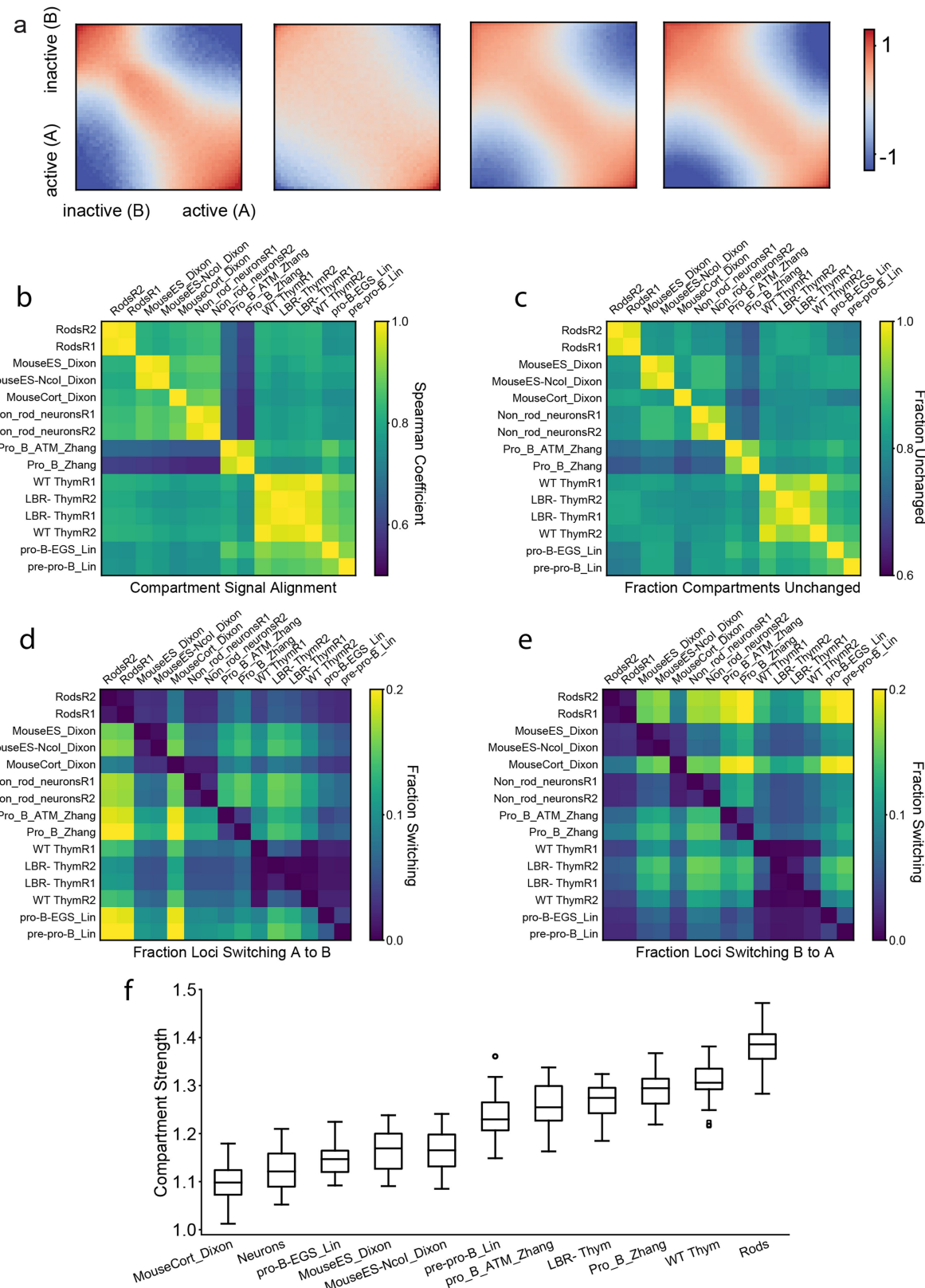
Extended Data Fig. 3 | Quantitative analysis of TADs. **a**, Average TADs, based on domain calls from embryonic stem cells³⁹. Ticks indicate start and end of TADs. The visual suggestion is that TADs are weakest in rods and strongest in non-rod neurons, with wild-type and *Lbr*^{-/-} thymocytes having intermediate strength. **b**, TAD strength is weakest in rods and strongest in non-rod neurons. TAD strength is the ratio of average contacts within the TAD (pink triangle) to average contacts between TADs (blue triangles). TAD strength is calculated separately for each autosome in two replicates. $n = 38$ chromosomes. Centre line is the median, the box ranges from the lower to upper quartiles and whiskers extend to 1.5× the interquartile range. **c**, Spearman correlation of insulation profiles across multiple mouse cell types, clustered hierarchically. Data were obtained from previous studies (GEO accession numbers GSE35156 and GSE63525)^{46,47}, as indicated by the name of the first author in the row and column labels. ES, embryonic stem cells. **d**, Average insulation profile (Methods) around TAD boundaries called in embryonic stem cells³⁹. The minimum insulation score of each profile is set to zero. We symmetrize noise by reflecting around the TAD boundary and averaging the reflected and original profiles. **e**, Decay of contact probability, $P(s)$, as a function of genomic separation, s . Shaded areas are bounded by $P(s)$ curves for biological replicates. All $P(s)$ curves are normalized to

their value at 10 kb. For rods, the steeper slope below 1 Mb and lack of a rollover in contrast to the other three cell types is indicative of weaker TADs, as previously described⁴⁸. **f**, TAD strength as a function of cell type (columns) and cell type from which TADs are called (rows). Data were obtained from previous studies (GEO accession numbers GSE98671, GSE63525 and GSE93431)^{39,47,48}, as indicated by the name of the first author in the row and column labels. Note that rods cluster with cell types with demonstrated weaker TADs. TAD strength is computed with the labavburst approach (see Methods). **g**, Average insulation profile (Methods) oriented around the top 10^4 scoring CTCF motifs. For scoring, we used the FIMO algorithm⁴⁹, with a position weight matrix for the M1 motif as previously described⁵⁰. The minimum insulation score of each profile is set to zero, and the CTCF motif points to the left. This provides a TAD-call independent method of inferring TAD strength, given that CTCF is frequently present at the borders of TADs. **h**, Snapshot of HiGlass⁵¹ view of the four datasets, close to the diagonal (chromosome 12: 77,538,523–85,180,785 and chromosome 12: 79,240,367–82,837,977; 32-kb resolution). Rods almost completely lack TADs and non-rod neurons have very strong TADs, upon inspection. Datasets can be browsed in a more in-depth fashion on the HiGlass website (<http://higlass.io/app/?config=JLOhiPILTmq6qDRicHMJqg>).



Extended Data Fig. 4 | Quantitative analysis of territories. **a**, Hi-C contact maps for chromosomes 1, 2 and 3 show both a checkerboard pattern in *cis* (within a chromosome) and *trans* (between chromosomes), reflecting compartmentalization, and more frequent *cis* than *trans* contacts, reflecting chromosome territoriality. Views are shown for the second biological replicate, binned at 500 kb. **b**, Average number of contacts between pairs of chromosomes. Average *cis* contacts are much higher than *trans* contacts. Maps are normalized by their sums. **c**, Average contacts in *trans*. For every unique pair of chromosomes, we averaged the first 60 Mb, binned at 500-kb resolution. Maps are normalized to their means and plotted in log-space. There is evidence of weak enrichment

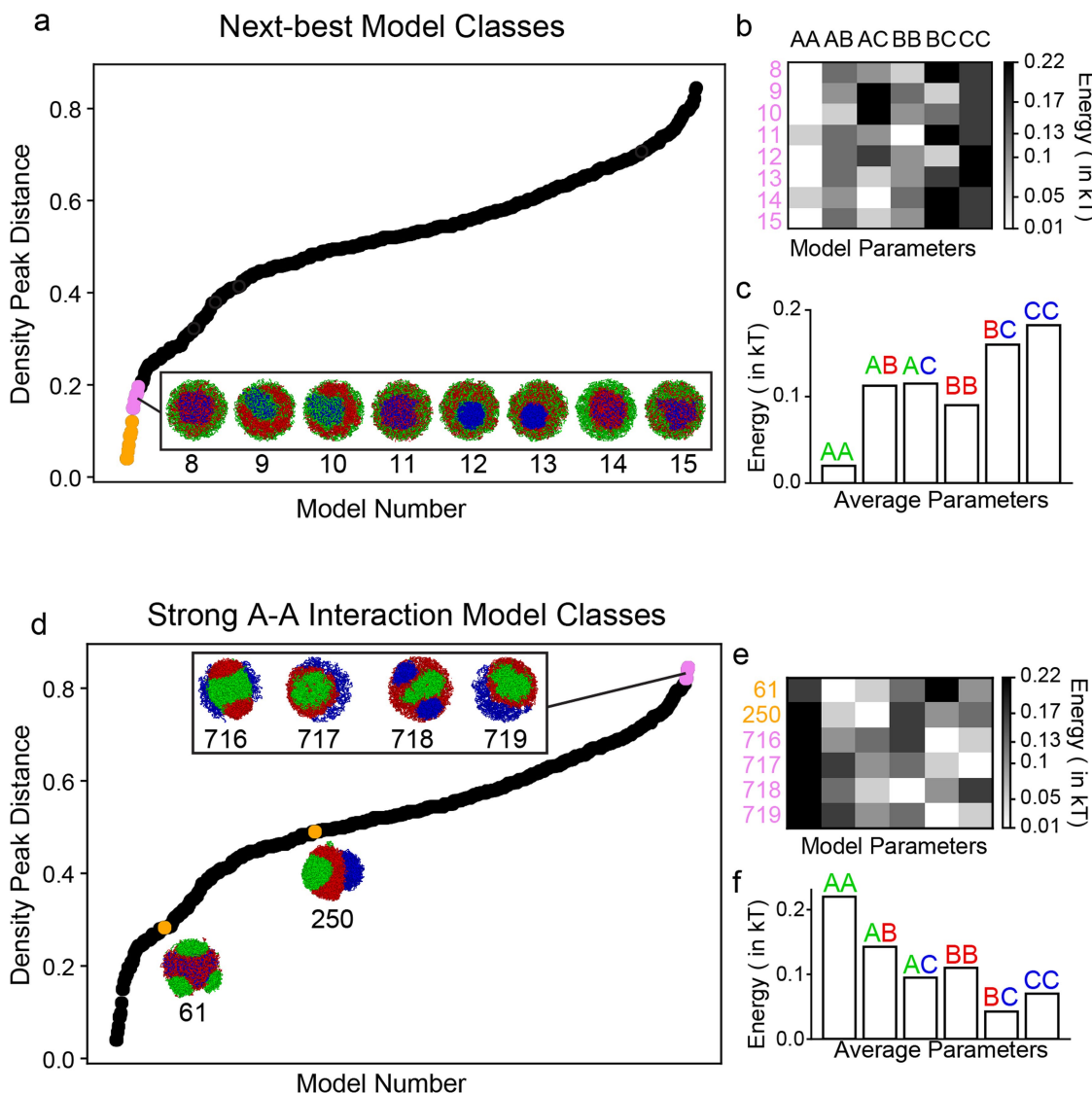
among chromocentre-proximal regions in *trans*, independent of inversion status. **d**, Consistent with the low *cis*-contact fraction revealed by Hi-C, chromosome 11 visualized by FISH (green) has a more diffuse territory in post-mitotic rods and non-rod neurons in comparison to cycling thymocytes of both genotypes. Projections of 2-μm confocal stacks. Scale bars, 5 μm. The chromosome painting was performed in four independent experiments. **e**, Chromosome territoriality, measured as the ratio of *cis* contacts to *cis* and *trans* contacts, is weaker in rods and non-rod neurons in comparison to conventional and inverted thymocytes. The schematic illustrates the compared regions. **f**, Scatterplot of compartmentalization and territoriality. The two metrics are not necessarily related.



Extended Data Fig. 5 | See next page for caption.

Extended Data Fig. 5 | Quantitative analysis of compartments. **a**, Saddle plots²³ (see Methods) of contact frequency enrichment show the extent of compartmentalization across cell types *in cis*. **b**, Spearman correlation of compartment profiles across multiple mouse cell types, clustered hierarchically. Data were obtained from previous studies (GEO accession numbers GSE35156, GSE35519 and GSE40173)^{46,52,53}, as indicated by the name of the first author in the row and column labels. Spearman's $r(LBR1, WT1) = 0.95, P < 1 \times 10^{-10}, n = 4,780$; $r(LBR1, LBR2) = 0.98, P < 1 \times 10^{-10}, n = 4,780$; $r(WT1, WT2) = 0.99, P < 1 \times 10^{-10}, n = 4,780$. P values are from two-sided tests. Positions of compartments are almost exactly the same between wild-type thymocytes and *Lbr*^{-/-} thymocytes,

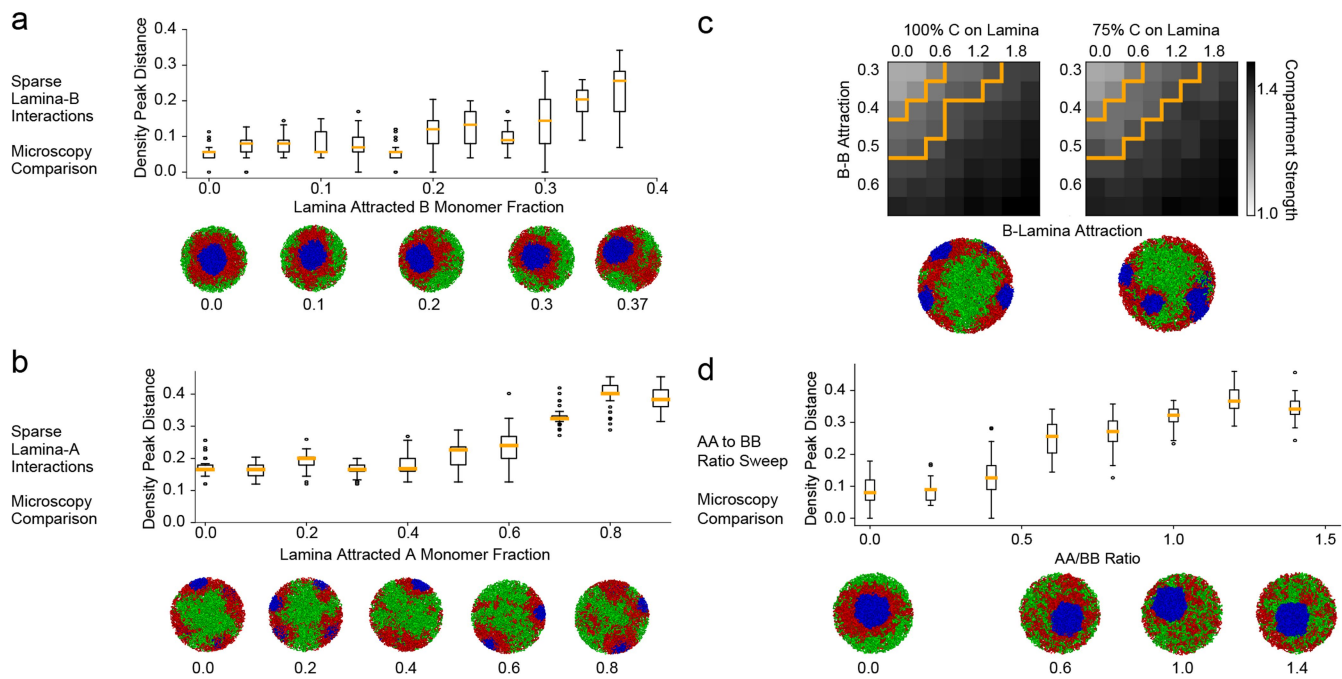
approaching that of biological replicates, which indicates that inversion does not change compartment positions as such. **c–e**, Fractions of loci that remain the same when comparing two different cell types, as well as fractions of loci that switched from B to A and from A to B. The sequence of cell types is taken from the clustering of their compartment profiles. **f**, Compartment strength across multiple mouse cell types (calculated separately for each autosome, $n = 19$ for datasets not considered in main text; $n = 38$ for two replicates of main text datasets. Centre line is the median, the box ranges from the lower to upper quartiles and whiskers extend to $1.5 \times$ the interquartile range.



Extended Data Fig. 6 | Exploring the space of model classes reveals that only a small fraction can reproduce the inverted nuclear geometry.

a, Even the second-best group of models do not display the ring-like structure that is characteristic of the inverted nucleus (the next-best eight models, indicated in pink, after the eight best models described in the main text, which are indicated in gold). Densities are computed from 50 simulated configurations. **b**, In agreement with the Flory–Huggins theory, we find that if the cross-type attraction (for example, A–B) is greater than both of the same-type attractions (A–A and B–B), the two monomer types will not segregate. For models 8, 11 and 15, this is true of both A–B and B–C terms, and as expected, there is mixing between A and B monomers, and B and C monomers in simulations. Similarly, models 9 and 10 have mixed A and C monomers and high A–C attraction; models 12 and 13 have mixed A and B monomers and higher A–B attraction; and model 14 has mixed B and C monomers, with high B–C attraction.

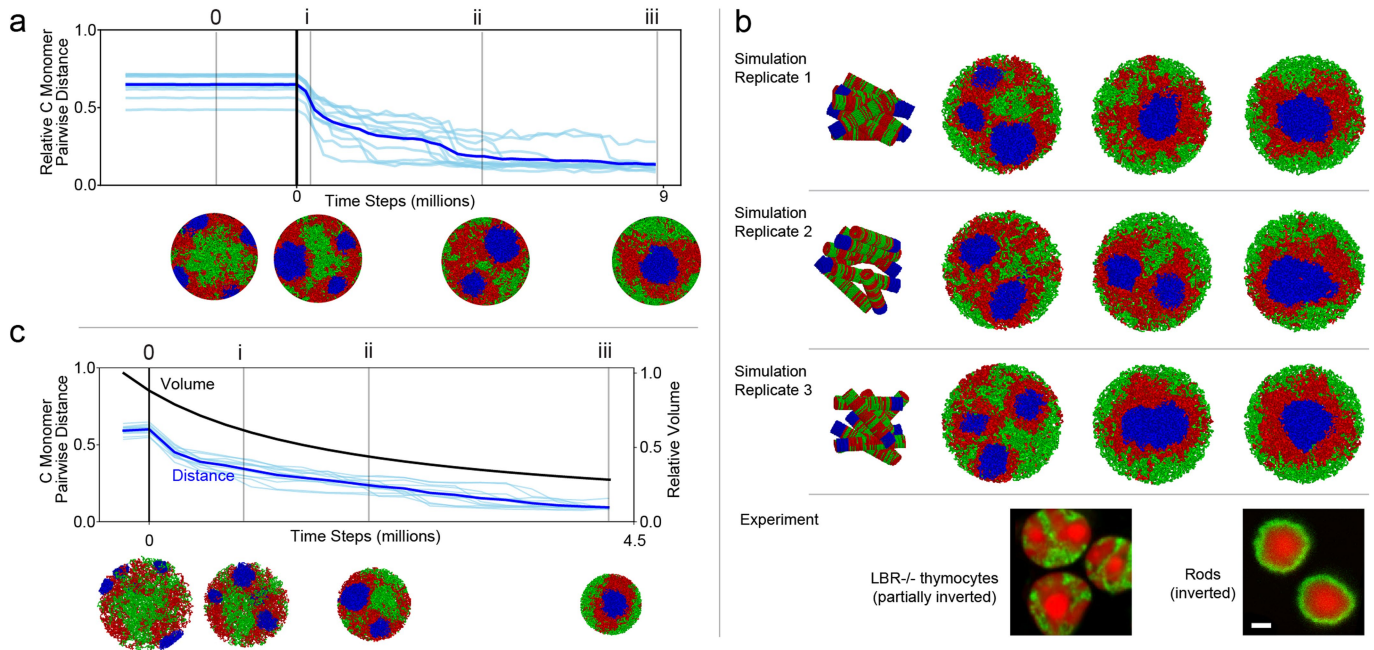
c, Averaging the parameter orders of the second-best model classes reveals that they depart from the best-performing models, in aggregate. **d**, We illustrate particular models with strong euchromatic interactions to show that such models do not compare well with microscopy, even on a quantitative level. In particular, we show the four worst-performing models (pink dots, models 716–719), all of which are characterized by strong euchromatic interactions (**b**). We also show the best-performing model with A–A as its strongest interaction (gold dot, model 250) and the best-performing model with A–A as its second strongest interaction (gold dot, model 61). Neither of these models compare well with experimental microscopy results. Densities are computed from 50 simulated configurations. **e**, All of the poorly performing models discussed in **d** were characterized by strong A–A interactions. **f**, Averaging the worst four models shows that they are characterized by strong A–A interactions.



Extended Data Fig. 7 | The heterochromatin-dominated model is robust to perturbations and outperforms a variety of alternative models.

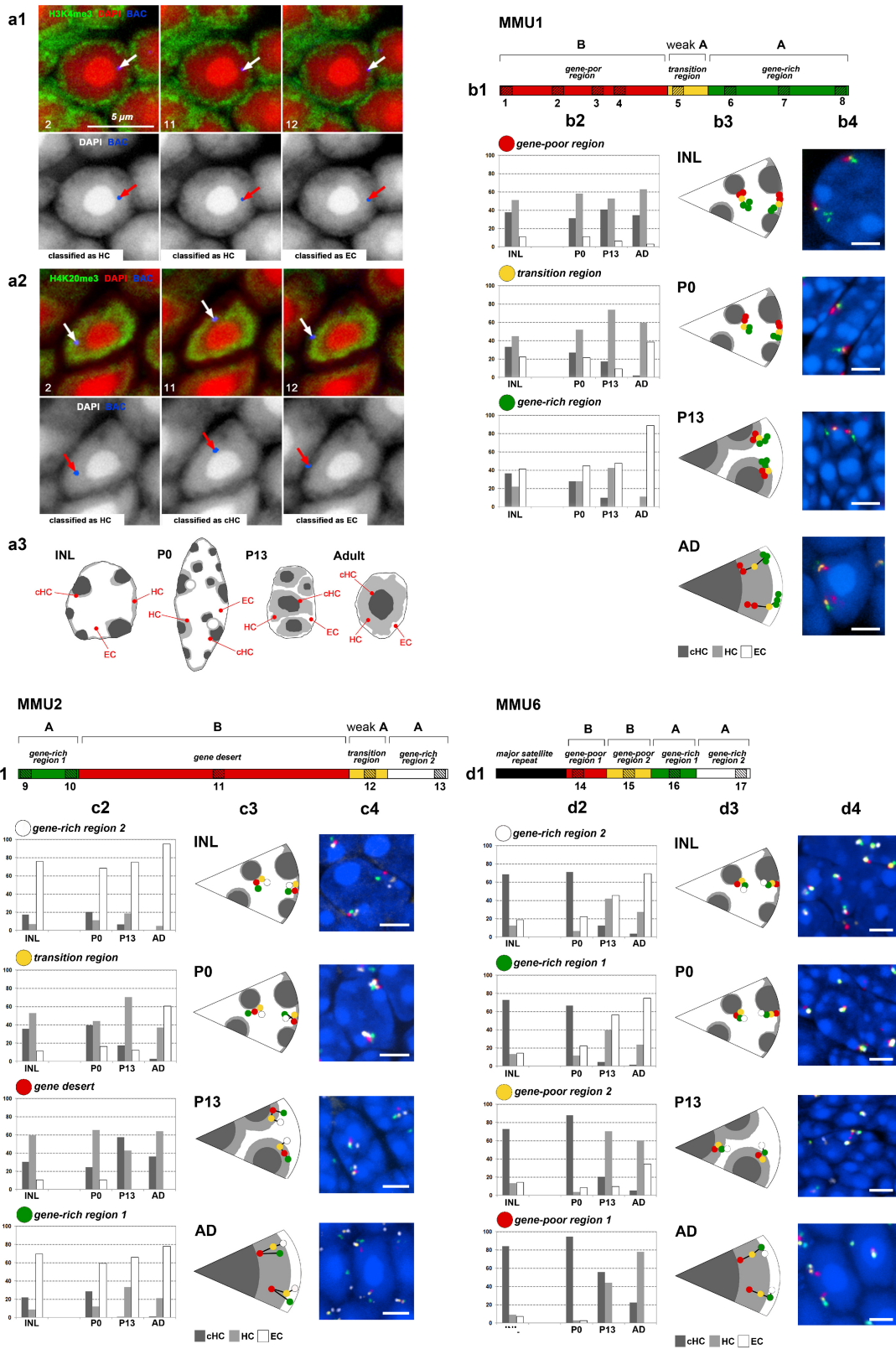
a, Adding in a fraction of B monomers attracted to the lamina, in an analogy to trace amounts of peripheral heterochromatin in rods⁵⁴, does not significantly change agreement with the microscopy results. Representative configurations as this fraction is increased are shown. Boxes indicate density peak distance with whiskers extending to 1.5× the interquartile range. $n = 50$, number of time points sampled across 3 simulation replicates. **b**, Adding in small fractions of A monomers attracted to the lamina (below 20%) does not significantly change the conventional morphology of simulated nuclei. Representative configurations as this fraction is increased are shown. Quantities plotted as in **a**. This simulation reflects a potential phenomenon of association between highly transcribed genes and nuclear pores. Of note, we have not observed this phenomenon in the nuclei of mouse cells, including rod cells, in which all euchromatin is adjacent to the nuclear lamina

(Supplementary Fig. 2). $n = 8$ simulated chromosomes. **c**, Average compartment strength across simulated chromosomes ($n = 8$) as a function of B-B and B-Lam attractions. The zone of parameter space for which simulated Hi-C compartment strength agrees with experimental compartment strength is essentially unchanged for simulations with some interior chromocentres, compared to simulations with no interior chromocentres. Representative configurations of each of these models are displayed. Orange outline indicates regions in parameter space for which the simulated Hi-C has compartmentalization in agreement with experimental Hi-C data (median ± 1 s.d. for wild-type thymocytes). **d**, For $B-B = 0.5$ and all other parameters as in the main text, increasing the ratio of A-A to B-B results in worse agreement with microscopy. This is particularly visible above $A-A/B-B = 0.5$. Representative configurations as this fraction is increased are shown. Quantities plotted as in **a**. $n = 8$ simulated chromosomes. Additional models are considered in Supplementary Fig. 6.



Extended Data Fig. 8 | Chromocentres merge during nuclear inversion and pass through a partially inverted morphology. **a**, Distance between chromocentres decreases once interactions with the lamina have been removed, quantitatively showing the fusion of C monomer droplets. To see this, we find the centre of mass of the C monomer blocks on each of the eight chromosomes in our simulation. We then compute the average distance between all possible pairs of the eight centres of mass, and normalize by the maximum possible total separation in the nucleus—that is, the diameter of the nucleus times the number of chromosome pairs. Light-blue lines show individual trajectories, the dark-blue line shows the average over trajectories. Following release from the lamina (vertical black line), this metric decreases, quantitatively confirming what we see visually in the associated configurations (numerals). **b**, Following three

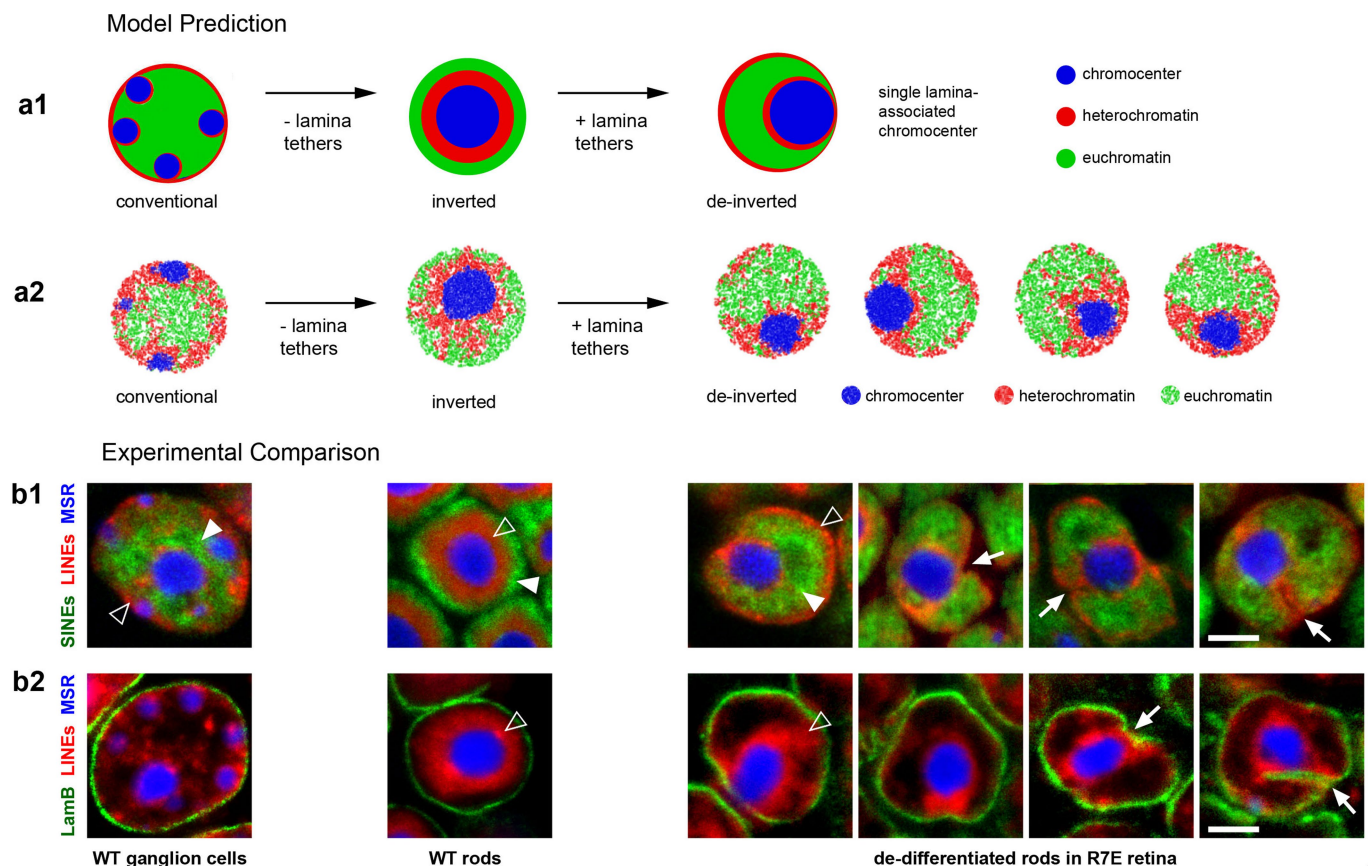
representative simulations starting from an initial condition in which chromosomes are in mitotic-like condensed cylindrical conformations, we find that our inverted nucleus model reaches its equilibrium configuration through a pathway that passes through a state highly reminiscent of the partial inversion seen in *Lbr^{-/-}* thymocytes. As a proxy for detailed mechanistic modelling of the complexities of mitotic exit, we begin from cylinders that are randomly oriented, as opposed to aligned. Scale bar, 2 μm . **c**, Distance between chromocentres decreases once interactions with the lamina have been removed, while the overall volume of the nucleus shrinks at the same time. Quantities plotted as in **a**, with an additional black line for volume decrease relative to initial volume. We see that the qualitative trends in morphology remain the same as in the case of constant volume (Fig. 4a).



Extended Data Fig. 9 | See next page for caption.

Extended Data Fig. 9 | Small chromosome segments faithfully localize to and move together with chromatin of their own compartment during nuclear inversion. The nuclear positions of short chromosome segments of different gene densities belonging to either the A or B compartment were studied using FISH with a cocktail of BAC probes on retinal cryosections at six developmental stages: P0, P6, P13, P21, P28 and adult (AD; 3.5 months). For the analysis of BAC signal distribution, three stages were considered: P0, with conventional nuclei of rod progenitors; P13, with rod nuclei in a transient state of inversion; and adult, with fully inverted rod nuclei. Cells with conventional nuclear organization in the inner nuclear layer (INL) of adult retina were used as a control. Between 100 and 120 alleles per chromosomal region were analysed. **a**, Immuno-FISH experiment showing how FISH signals were classified according to their localization in the three major nuclear zones. EC, euchromatin; HC, heterochromatin; cHC, constitutive heterochromatin. Definitions of these three types of chromatin have been previously published¹. BAC 12 maps to the most peripheral euchromatic shell of the rod nucleus stained with anti-H3K4me3 antibody. This nuclear zone is adjacent to the nuclear periphery and contains the genic part of the mouse genome (see Supplementary Fig. 2). BACs 2 and 11 are located in the heterochromatic zone of the nucleus encircling the chromocentre and stained with anti-H4K20me3 antibody. Thus, classification of BAC signals based on DAPI staining is justified by immunostaining of histone modifications and

enables the signal distribution analysis described in **b–d**. Top, localization of BAC signals (blue, white arrows) and histone modifications (green) in DAPI-counterstained nuclei (red). Numbers in the lower left corners indicate the BAC numbers (for their coordinates, see Methods). Bottom, greyscale images of DAPI and positions of the BAC signals (red arrows) represented by false-coloured mask. **b–d**, Analysis of BAC signal positions after FISH with BAC cocktail probes mapping to selected chromosome regions. Top, schematics of the chromosome regions on MMU1 (**b**), MMU2 (**c**) and MMU6 (**d**). The coloured segments differ in their gene content and assignment to either the A or B compartment. The striped boxes with numbers below indicate the BACs used for FISH. Bottom left, graphs showing the distribution of the segments within rod nuclei at the three developmental stages and adult cells of the inner nuclear layer. The bars represent the proportion of signals in each nuclear zone: adjacent to constitutive heterochromatin (dark grey), within heterochromatin (light grey) and within euchromatin (white). Bottom middle, schematics showing typical segment distribution of the studied regions. Bottom right, representative nuclei after three-colour (**b**) or four-colour (**c, d**) FISH. The images are maximum-intensity projections of short (1.4–2-μm) stacks. False colours assigned to segments correspond to the colour code used in each panel. The experiment was repeated twice. For an example of the localization of a single gene and its movement together with chromatin of the A compartment during nuclear inversion, see Supplementary Fig. 3.



Extended Data Fig. 10 | Coalescence of individual chromocentres into a large central chromocentre is irreversible. **a**, Top, our model predicts that once nuclei invert and all individual chromocentres merge into a single central chromocentre, the reverse process—that is, resplitting into smaller chromocentres—will not take place after the reintroduction of lamina attractions. Although we expect B monomers to redistribute to the nuclear lamina, we do not expect C monomers of a single globule to reorganize into smaller globules. In this sense, our model predicts that the inversion and formation of the central chromocentre is irreversible. Bottom, simulations of de-inversion of inverted nuclei through the introduction of B-Lam and C-Lam attractions with strengths equal to the optimal B-Lam value from Fig. 3c, d. Note that according to our prediction, de-inverted nuclei only partially return to the conventional geometry. Slices with a thickness of 5% of the nuclear diameter are shown. **b**, In agreement with the model prediction, de-inverted nuclei do not return to a typical conventional architecture, as can be seen in de-differentiated rods of R7E mice expressing poly(Q)-expanded ataxin-7 (see Supplementary Fig. 5a, b for a description of the phenotype). FISH with probes for major

satellite repeats (blue), LINE-rich heterochromatin (red) and SINE-rich euchromatin (green) demonstrates that although euchromatin returns to the nuclear interior (filled arrowheads) and heterochromatin repositions to the lamina (empty arrowheads), a single large chromocentre remains and is typically positioned at the nuclear periphery (top, arrows). Notably, in approximately 30% of the nuclei, the large chromocentre does not relocate to the nuclear periphery but the nuclear lamina (green) makes deep narrow invaginations, contacting the chromocentre (bottom, arrows; see also Supplementary Fig. 5c). The remaining bulky chromocentre is surrounded by LINE-rich chromatin (bottom; empty arrowheads) and is often (71% of nuclei) in contact with the nuclear periphery as a result of deformation of nuclear shape (for more examples, see Supplementary Fig. 5c). For comparison, the two left columns show conventional nuclei of ganglion cells and inverted rod nuclei from a wild-type mouse. Images are single optical sections. Scale bars, 2 μ m; scale bars apply to all images. Probes, FISH and microscopy are described in the Methods. Each experiment was repeated three times.

Corresponding author(s): Leonid Mirny, Irina Solovei

Initial submission Revised version Final submission

Life Sciences Reporting Summary

Nature Research wishes to improve the reproducibility of the work that we publish. This form is intended for publication with all accepted life science papers and provides structure for consistency and transparency in reporting. Every life science submission will use this form; some list items might not apply to an individual manuscript, but all fields must be completed for clarity.

For further information on the points included in this form, see [Reporting Life Sciences Research](#). For further information on Nature Research policies, including our [data availability policy](#), see [Authors & Referees](#) and the [Editorial Policy Checklist](#).

► Experimental design

1. Sample size

Describe how sample size was determined.

We used 2 biological replicates for Hi-C analysis of all cell types (rods, non-rod neurons, WT and LBR-null thymocytes).
For each rod cell and non-rod neuron replicate (1 - 10 mln cells), we used retinas from 2 and 3 mice, respectively.
For each thymocyte replicate (40 - 60 mln cells) we used thymus from 1 mouse.

2. Data exclusions

Describe any data exclusions.

No data were excluded from the analysis

3. Replication

Describe whether the experimental findings were reliably reproduced.

All replication attempts were successful

4. Randomization

Describe how samples/organisms/participants were allocated into experimental groups.

We did not perform experiments requiring sample randomization. Differences between data sets were stark enough that visual identification was obvious.

5. Blinding

Describe whether the investigators were blinded to group allocation during data collection and/or analysis.

Experiments were not blinded. Differences between data sets were stark enough that visual identification was obvious upon viewing data.

Note: all studies involving animals and/or human research participants must disclose whether blinding and randomization were used.

6. Statistical parameters

For all figures and tables that use statistical methods, confirm that the following items are present in relevant figure legends (or in the Methods section if additional space is needed).

n/a Confirmed

- The exact sample size (*n*) for each experimental group/condition, given as a discrete number and unit of measurement (animals, litters, cultures, etc.)
- A description of how samples were collected, noting whether measurements were taken from distinct samples or whether the same sample was measured repeatedly
- A statement indicating how many times each experiment was replicated
- The statistical test(s) used and whether they are one- or two-sided (note: only common tests should be described solely by name; more complex techniques should be described in the Methods section)
- A description of any assumptions or corrections, such as an adjustment for multiple comparisons
- The test results (e.g. *P* values) given as exact values whenever possible and with confidence intervals noted
- A clear description of statistics including central tendency (e.g. median, mean) and variation (e.g. standard deviation, interquartile range)
- Clearly defined error bars

See the web collection on [statistics for biologists](#) for further resources and guidance.

► Software

Policy information about [availability of computer code](#)

7. Software

Describe the software used to analyze the data in this study.

Software used to store and analyze Hi-C data can be accessed at <https://bitbucket.org/mirnylab/hiclib> and <https://bitbucket.org/mirnylab/mirnylib>. Data was also stored using the Cooler software (<https://github.com/mirnylab/cooler>). Simulations were performed with OpenMM v7.2.2 and CUDA v9.1.85. Analysis of data was done with NumPy v1.15.1.

For manuscripts utilizing custom algorithms or software that are central to the paper but not yet described in the published literature, software must be made available to editors and reviewers upon request. We strongly encourage code deposition in a community repository (e.g. GitHub). *Nature Methods* guidance for [providing algorithms and software for publication](#) provides further information on this topic.

► Materials and reagents

Policy information about [availability of materials](#)

8. Materials availability

Indicate whether there are restrictions on availability of unique materials or if these materials are only available for distribution by a for-profit company.

No unique materials have been used.

9. Antibodies

Describe the antibodies used and how they were validated for use in the system under study (i.e. assay and species).

=====
 Primary antibodies
 =====
 H4K8ac (72A9, 5.8 µg/µl, 1:200), anti-H4K20me3 (27F10, 5.6 µg/µl, 1:200), H3K9ac (2F3, 3.4 µg/µl, 1:200) - provided by Hiroshi Kimura (described/validated in 10.10 (38/jhg.2013.66 and 10.1007/s10577-013-9375-7)
 H3K4me3 (Abcam, ab8580, 1:100)
 H3S10ph (Abcam, ab14955, 1:1000)
 Ki67 (Abcam, ab15580, 1:200)
 Rhodopsin (Abcam, ab3267, clone RET-P1, 1:500)
 Lamin A/C (LAZ, serum, undiluted) - provided by Harald Herrmann (described/validated in 10.1007/s00109-007-0275-1)
 Lamin B1 (Santa Cruz Biotechnology, SC6217, clone M-20, 1:100)
 Nup153 (Abcam, ab24700, QE5, 1:100)
 ATAXN7 (1261, 1:100) - provided by Didier Devys (described/validated in 10.1093/hmg/ddh139)
 =====
 Secondary antibodies
 =====
 Mouse-anti-Dig antibody conjugated to FITC (Jackson Immuno Research, 200-092-156, 1:100)
 Donkey-anti-mouse conjugated to Alexa488 (Invitrogen, A11001, 1:500)
 Donkey-anti-mouse conjugated to Alexa555 (Invitrogen, A31570, 1:500)
 Donkey-anti-mouse conjugated to Alexa594 (Invitrogen, A21203, 1:500)
 Donkey-anti-mouse conjugated to Alexa647 (Invitrogen, A31571, 1:500)
 Donkey-anti-rabbit conjugated to Alexa488 (JacksonImmuno Research, 711-547-003, 1:500)
 Donkey-anti-rabbit conjugated to Alexa555 (Invitrogen, A31572, 1:500)
 Donkey-anti-rabbit conjugated to Alexa649 (JacksonImmuno Research, 711-496-152, 1:500)

10. Eukaryotic cell lines

- State the source of each eukaryotic cell line used.
- Describe the method of cell line authentication used.
- Report whether the cell lines were tested for mycoplasma contamination.
- If any of the cell lines used are listed in the database of commonly misidentified cell lines maintained by [ICLAC](#), provide a scientific rationale for their use.

No eukaryotic cell lines were used in this study.

No eukaryotic cell lines were used in this study.

No eukaryotic cell lines were used in this study.

No eukaryotic cell lines were used in this study.

► Animals and human research participants

Policy information about [studies involving animals](#); when reporting animal research, follow the [ARRIVE guidelines](#)

11. Description of research animals

Provide details on animals and/or animal-derived materials used in the study.

- (1) For sampling of rods and WT thymocytes for Hi-C, we used female adult mice (retired breeders) of CD1 strain (<https://www.criver.com/products-services/find-model/cd-1-igs-mouse?region=23>).
 - (2) For sampling of non-rod neurons for Hi-C, we used female adult mice (2 month old) of C3H strain (<https://www.criver.com/products-services/find-model/c3h-mouse?region=23>).
 - (3) For sampling of LBR-null thymocytes for Hi-C, we used female adult (3 and 4 month old) LBR GT/GT mice (10.1093/hmg/ddn191).
 - (4) For the FISH and immunostaining experiments we used retinas of CD1 mice at different stages of development (P0, P3, P6, P13, P21, P28) and adults (14 weeks).
 - (5) For immuno-FISH in ATAXN7 retinas, retina samples from R7E mice (4, 6, 20, 70 and 93 week old) were provided by Didier Devys (10.1371/journal.pbio.0040067; 10.1016/j.cell.2013.01.009)
- Other details are given in the Methods section.

Policy information about [studies involving human research participants](#)

12. Description of human research participants

Describe the covariate-relevant population characteristics of the human research participants.

The study did not involve human participants